A THEORETICAL AND EXPERIMENTAL STUDY OF THE SLOW

VISCOUSLY DRIVEN MOTION OF A BAROTROPIC FLUID IN A

RAPIDLY ROTATING CYLINDER WITH SLOPING BOTTOM

by

ROBERT CRUCE BEARDSLEY

B.S., Massachusetts Institute of
Technology

Submitted in partial fulfillment
of the requirements for the
degree of doctor of
science
at the

Massachusetts Institute of Technology

January, 1968

Signature of Author......................................
Department of Geology and
Geophysics, January 8, 1968

Certified by..
Thesis Supervisor

Accepted by..
Chairman, Departmental
Committee on Graduate
Students

Lindgren

A Theoretical and Experimental Study of the Slow Viscously Driven Motion of a Barotropic Fluid in a Rapidly Rotating Cylinder with Sloping Bottom

by
Robert C. Beardsley

A simple laboratory model for the wind-driven ocean circulation is studied both theoretically and experimentally. A right cylinder rotating about its vertical axis with angular velocity Ω holds a homogeneous fluid of viscosity ν between two planes, formed by non-parallel end plates with an average separation L. The fluid is driven by the steady rotation of the horizontal lid about the cylinder axis with angular velocity $(1 + \epsilon)\Omega$. The sloping bottom intersects the cylinder at an angle α and is stationary relative to the cylindrical side wall. A linear theory is developed for the interior and side wall boundary layer structures for the case of bottom slope $\tan\alpha$ from 0 to 0(1), where the results of Pedlosky and Greenspan (1967) are extended to second order in $\tan\alpha$ to close the vertical mass flux. Interior and boundary layer velocity measurements are presented for $\alpha \sim 6°$, $8°$, and $10°$, obtained over the range of Ekman number $E = \nu/\Omega L^2$ from 1.05 x 10^{-5} to 6.22 x 10^{-5}, and Rossby number ϵ from -.0015 to -.1591. These agree well with theory when the parameter $\epsilon/E^{1/2}$ is of order one or less. The western side wall boundary layer showed downstream intensification when $\epsilon/E^{1/2}$ is increased and topographic "Rossby" waves appear in the transition region where the western side wall layer terminates. The motion becomes unstable with the critical value $\epsilon/E^{1/2}$ is reached independent of $\tan\alpha$ and a large scale low frequency oscillation is observed. A brief comparison is made with previous wind-driven ocean circulation model studies.

Thesis Supervisor: Raymond Hide
Title: Professor, Department of Geology and Geophysics

iii

TABLE OF CONTENTS

FIGURES

v

TABLES

vi

PLATES

1. Introduction

This paper considers the slow viscously-driven motion of an imcompressible homogeneous fluid in a rapidly rotating right cylinder with sloping bottom. The lower surface is formed by a plane intersecting the cylinder at an angle α. The upper surface is normal to the cylinder axis and rotates steadily with an angular velocity $(1 + \epsilon)\Omega$, while the rest of the fluid container rotates with Ω (see Fig. 1).

This model was recently presented by Pedlosky and Greenspan (1967) to demonstrate how the general theory of Greenspan (1965) for nearly rigid rotating flows must be modified for a fluid container like the sliced cylinder which possesses no closed geostrophic contours. An additional feature of this model is the similarity of its solution to the large scale ocean circulation. The physical analogy between vortex stretching by motion across the bottom contours and the creation of relative vorticity by the northward increase in horizontal Coriolis acceleration (the β-effect) enables the sliced cylinder to replicate several important features of the wind-driven ocean circulation problem. The analysis of Pedlosky and Greenspan showed that the symmetric character of the flow obtained when $\alpha = 0$ is completely changed by the bottom slope when α is small but greater than $E^{\frac{1}{2}}$, where E is the Ekman number $\nu / \Omega L^2$. A finite bottom slope constrains the interior flow to a slow $O(E^{\frac{1}{2}})$ drift across the depth contours which is closed by a strong $O(E^{\frac{1}{6}})$ viscous non-axially symmetric boundary layer along the western side wall.

The purpose of this paper is to re-examine the sliced cylinder model both theoretically and experimentally. A linear theory is developed in Section 2 for the interior and vertical boundary layer structure for the intermediate cases from tan $\alpha = 0$ to $O(1)$, where the results of Pedlosky and Greenspan are extended to close the vertical circulation. Section 3 contains a description of the experimental apparatus and techniques . The results of velocity measurements are presented in Section 4 for $\alpha \simeq 6°$,
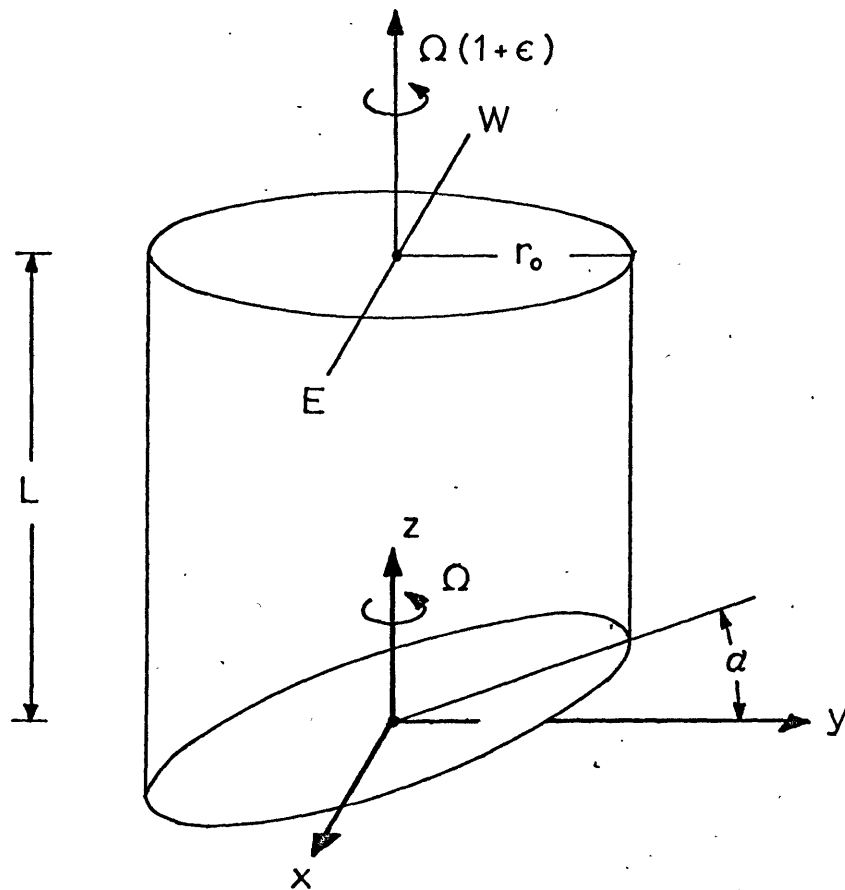
FIGURE 1. Schematic diagram of basin

$8°$, and $10°$, obtained over the range of Ekman number from 1.05×10^{-5} to 6.22×10^{-5} and Rossby number ϵ from $-.0015$ to $-.1591$. A brief comparison between the sliced cylinder model and recent wind-driven ocean circulation model-studies will be presented in the finals section in the final section.

2. Theoretical Development

The mathematical analysis of the steady motion in the sliced cylinder configuration shown in Fig. 1 is formulated following the approach outlined by Greenspan (1965). The governing equations are the linearized momentum and continuity equations for an incompressible fluid of constant density ρ and viscosity ν, written in a coordinate system rotating with the cylinder at an angular velocity Ω,

$$2\hat{k} \times \vec{u} = -\nabla p + E\nabla^2 \vec{u} \tag{1}$$
$$\nabla \cdot \vec{u} = 0$$

and scaled with respect to the container's mean depth L and the lid's relative angular velocity $\epsilon\Omega$. The unprimed non-dimensional field variables are

$$\vec{r}' = L\vec{r} \ , \ \vec{u}' = \epsilon\Omega L \vec{u} \ , \ p' = \rho\epsilon(\Omega L)^2 p \ , \ t = \epsilon\Omega t' , E = \nu/\Omega L^2$$

The scaled boundary conditions on the velocity field are then

$$\text{top: } v(r,\theta,1) = r, \ u = 0 \ , \ w = 0 \tag{2a}$$
$$\text{side: } \vec{u}(a,\theta,z) = 0 \tag{2b}$$
$$\text{bottom: } \vec{u}(r,\theta,\tan\alpha y) = 0 \tag{2c}$$

Since our primary interest lies in the dependence of the interior flow and viscous side wall boundary layer structure on the value of α, we will not solve explicitly for the flow in either top or bottom Ekman layers but will use instead a general implicit solution for the Ekman layer suction. Greenspan and Howard (1963) and Greenspan (1965) have previously shown that the effect of an Ekman layer developed on a smooth boundary on the interior flow can be expressed in a compatibility condition on the interior variables

$$\hat{n} \cdot \vec{u} = \frac{E^{1/2}}{2|\hat{n} \cdot \hat{k}|^{1/2}} \; \hat{n} \cdot \nabla \times \left\{ \hat{n} \times (\vec{u} - \vec{u}^*) + \frac{\hat{n} \cdot \hat{k}}{|\hat{n} \cdot \hat{k}|} (\vec{u} - \vec{u}^*) \right\} \quad (3)$$

where $\hat{n}$ is the outward unit normal to the container surface and $\vec{u}^*$ is the relative velocity of that surface. On the upper surface of the sliced cylinder, $\hat{n} = \hat{k}$ and $\vec{u}^* = \Lambda \hat{\theta}$ so (2a) becomes

$$\omega = -\frac{E^{1/2}}{2} \left\{ \hat{k} \cdot \nabla \times \vec{u} - 2 \right\} \quad \text{at} \quad z = 1 \quad (4)$$

while on the sloping bottom, the outward normal is $\hat{n} = \sin\alpha \, \hat{j}$ $- \cos\alpha \, \hat{k}$, causing (2c) to become

$$\omega = \tan\alpha \; \hat{j} \cdot \vec{u} + \frac{E^{1/2}}{2} \left\{ \hat{k} \cdot \nabla \times u + O(\tan^2\alpha) \right\} \quad (5)$$

The $\tan\alpha$ term represents the imposed vertical velocity of a fluid element moving parallel to the bottom incline. Ignoring the $O(E^{1/2}\tan^2\alpha)$ terms for small α , the vertical velocity above the bottom Ekman layer consists of an "orographic" component plus the Ekman layer flux. We shall see that as α increases from 0, the constraint imposed by the increasing orographic component essentially determines the character of the complete flow.

Case 1: $\tan\alpha = 0$.

While the solution in this case is well known, it is instructive to reconsider it briefly. Zero slope makes the container symmetric in shape so an axi-symmetric response is expected. A vertical axi-symmetric stream function χ can then be introduced, the velocity field being

$$\vec{u} = -\nabla \times \left\{ \chi(\Lambda, z) \hat{\theta} \right\} + v(\Lambda, z) \hat{\theta}$$

The $\hat{\theta}$-components of the momentum and vorticity balances form a coupled set of partial differential equations for χ and v,

$$2\chi_z - ED v = 0 \quad (6a)$$
$$2v_z + EDD \chi = 0 \quad (6b)$$

where D is the cylindrical differential operator

$$D\psi = \psi_{\Lambda\Lambda} + \frac{\psi_\Lambda}{\Lambda} - \frac{\psi}{\Lambda^2} + \psi_{zz}$$

The boundary conditions on χ and v are set by no-slip at the side wall and the Ekman layer fluxes. The first is given by

$$u(a,z) = \chi_z = 0$$
$$w(a,z) = -\chi_{\scriptscriptstyle \wedge} - \frac{\chi}{\scriptstyle \wedge} = 0$$
$$v(a,z) = 0$$

The vertical flux into the upper Ekman layer is given by the compatability condition (3)

$$w(\scriptstyle \wedge,1) = -\frac{1}{\scriptstyle \wedge}(\scriptstyle \wedge \chi)_{\scriptstyle \wedge} = \frac{E^{1/2}}{2}\frac{1}{\scriptstyle \wedge}(\scriptstyle \wedge(\scriptstyle \wedge - v))_{\scriptstyle \wedge}$$

This expression may be directly integrated to give the total flux per radian into the top layer

$$\int_0^{\scriptstyle \wedge} w(\scriptstyle \wedge',1)\,\scriptstyle \wedge'\,d\scriptstyle \wedge' = -\scriptstyle \wedge\chi(\scriptstyle \wedge,1) = \frac{\scriptstyle \wedge E^{1/2}}{2}(\scriptstyle \wedge - v)$$

The resulting condition on χ is then

$$\chi(\scriptstyle \wedge,1) = -\frac{E^{1/2}}{2}(\scriptstyle \wedge - v)$$

where the explicit $\scriptstyle \wedge$ in the right hand side represents the forcing transmitted by the upper Ekman layer. $\chi(\scriptstyle \wedge, 0)$ just above the lower Ekman layer is found in the same manner to be

$$\chi(\scriptstyle \wedge,0) = -\frac{E^{1/2}\,v}{2}$$

Since viscous stresses in the interior are small, O(E), the interior dynamics are geostrophic with a balance berween Coriolis acceleration and the horizontal pressure gradient. The steady flow by (6) is independent of z as a consequence of geostrophy in a barotropic fluid (known as the Proudman-Taylor theorem) so the top Ekman layer suction must be supplied by an outflux from the lower Ekman layer. Matching fluxes requires

$$\chi(\scriptstyle \wedge,1) = \chi(\scriptstyle \wedge,0)$$
$$\therefore \quad v(\scriptstyle \wedge) = \scriptstyle \wedge/2$$

The interior motion is the well-known solid body rotation with an angular velocity equal to the arithmetic mean of the rotation rates of the top and bottom plates.

The side wall flow can be found by boundary layer methods. The interior flow near the side wall is an O(1) tangential flow. The only term in the $\hat{\theta}$-momentum equation capable of balancing the viscous force necessary to bring v to zero at the side wall

is the Coriolis component $2u$. The existence of closed stream-lines implies $O(u) \sim O(\chi) \sim E^{\frac{1}{2}}$ near the side wall. Then $O(E \, v_{\lambda\lambda}) \sim E^{\frac{1}{2}}$ for a dynamic balance. Since $O(v) \sim 1$, $O(\frac{\partial}{\partial r}) \sim E^{-\frac{1}{4}}$, indicating that a boundary layer with scale thickness $E^{\frac{1}{4}}$ is required to satis- fy the non-slip condition on the $O(1)$ azimuthal flow.

The coupled set (6) may also be reduced to the sixth order partial differential equation,

$$\left\{ E^2 DDD + 4 \frac{\partial^2}{\partial z^2} \right\} \begin{bmatrix} \chi \\ v \end{bmatrix} = 0 \qquad (7)$$

A balance here requires $O(E^2 \frac{\partial^6}{\partial \lambda^6}) \sim 1$, indicating that a second boundary layer of thickness $E^{\frac{1}{3}}$ may also be needed to match the lateral boundary conditions.

Having determined the possible side wall boundary layer thicknesses, we now seek consistent perturbation expansions for χ and v valid outside the Ekman layers. The ratio of boundary layer thicknesses $E^{\frac{1}{3}} / E^{\frac{1}{4}} = E^{\frac{1}{12}}$ provides an appropriate expansion parameter so we will assume expansions of the form

$$v = \sum_{n=0} E^{n/12} \, v_n (\lambda, z)$$
$$\chi = \sum_{n=6} E^{n/12} \, \chi_n (\lambda, z)$$

and seek solutions for the functions v_n, χ_n. The analysis is simplified by introducing stretched coordinates in the vertical boundary layers

$$a - \lambda = E^{\frac{1}{3}} \eta = E^{\frac{1}{4}} \zeta. \qquad (8)$$

Substituting these expansions into the basic equations and equating coefficients of like powers of $E^{\frac{1}{12}}$ lead to a sequence of problems for the unknown functions in each area.

The interior solution is again $v_0 = \lambda/2$, $\chi_0 = -\lambda/4$, a geostrophic gyre with a parabolic pressure field, coupled with a slow $E^{\frac{1}{2}}/2$ uniform vertical flux from the lower into the upper Ekman layer. The return of this flux to close the vertical circu- lation must be made via the vertical boundary layers on the side wall.

The problem sequence in the $E^{\frac{1}{4}}$ layer reduces to

$$v_{0\zeta\zeta} - 2\chi_{6z} = 0 \qquad (9a)$$

$$v_{0z} = 0 \qquad (9b)$$

with the associated no-slip and flux conditions

$$v_0(0, z) = 0$$

$$\chi_6(\zeta, 1) = \frac{v_0 - a}{2}$$

$$\chi_6(\zeta, 0) = -\frac{v_0}{2}$$

The Proudman-Taylor effect strongly influences the $E^{\frac{1}{4}}$ layer flow. The horizontal motion remains two-dimensional, allowing the θ-momentum equation $(9a)$ to be vertically integrated and χ_6 evaluated at $z = 1, 0$. This yields the ordinary differential equation

$$v_{0\zeta\zeta} - 2v_0 = -a$$

Its solution subject to no-slip is

$$v_0 = \frac{a}{2}\left(1 - e^{-\sqrt{2}\zeta}\right)$$

With the corresponding streamfunction

$$\chi_6 = -\frac{a}{4}\left(1 - (2z - 1)e^{-\sqrt{2}\zeta}\right)$$

the vertical flux is

$$w = E^{1/4}\frac{a\sqrt{2}}{4}(2z - 1)e^{-\sqrt{2}\zeta}$$

The horizontal shear is great enough in the $E^{\frac{1}{4}}$ layer to cause both Ekman layers to extract fluid from the $E^{\frac{1}{4}}$ layer.

The $E^{1/3}$ layer flow is both ageostrophic and three-dimensional. The lower order flow must be found by matching the already determined $E^{\frac{1}{4}}$ layer solutions to the $E^{1/3}$ layer solutions yet to be determined. This is accomplished formally by expanding the $E^{\frac{1}{4}}$ layer solutions in terms of the $E^{1/3}$ layer coordinate and then matching coefficients with the $E^{1/3}$ layer solutions for equal powers of $E^{1/12}$. This procedure identifies

$$v_0 = 0$$

$$v_1 = \frac{a}{\sqrt{2}}\eta$$

The governing equation for the next order flow is

$$\left\{\frac{\partial^6}{\partial\eta^6} + 4\frac{\partial^2}{\partial z^2}\right\}\begin{bmatrix}\chi_6 \\ v_2\end{bmatrix} = 0 \qquad (10)$$

The boundary conditions are the lowest order Ekman flux conditions

$$\chi_6(\eta, 1) = -\frac{a}{2}$$
$$\chi_6(\eta, 0) = 0$$

which are equivalent to setting $w = E^{1/6} w_2 = 0$ since the Ekman flux out of the $E^{1/3}$ layer is of $O(E^{1/3})$. The no-slip condition at the side wall is

$$\hat{\lambda}: \quad \chi_6(0,z) - \frac{az}{2} = 0 \tag{11a}$$

$$\hat{\theta}: \quad \chi_{6\eta\eta\eta} = 0 \tag{11b}$$

$$\hat{k}: \quad \chi_{6\eta} = 0 \tag{11c}$$

where the second term in (11a) is the $E^{1/4}$ layer radial flux. A sine series solution for χ_6 can be found directly, giving the complete streamfunction and azimuthal velocity in the $E^{1/3}$ layer to order $O(E^{1/6})$,

$$v(\eta,z) = \frac{E^{1/12}}{\sqrt{2}} a\eta + E^{1/6}\left\{ -\frac{a\eta^2}{2} + \sum_{m=1} \frac{2a}{\sqrt{3}} \frac{(-1)^m \gamma_m}{m\pi} e^{-\frac{\gamma_m \eta}{2}} \sin\left(\frac{\sqrt{3}\gamma_m\eta}{2}\right) \cos m\pi z \right\} \tag{12a}$$

$$\chi(\eta,z) = E^{1/2}\left\{ -\frac{az}{2} + \sum_{m=1} \frac{2}{\sqrt{3}} \frac{a(-1)^{m+1}}{m\pi} e^{-\frac{\gamma_m \eta}{2}} \sin\left(\frac{\sqrt{3}\gamma_m\eta}{2} + \frac{\pi}{3}\right) \sin m\pi z \right\} \tag{12b}$$

where $\gamma_m = (2m\pi)^{1/3}$, the magnitude of the eigenvalues of (10).

These solutions for the lowest order flow in both layers account for the basic viscous mechanism of bringing the $O(1)$ azimuthal flow to rest and closing the vertical mass flux. Large horizontal shear in the $E^{1/4}$ layer makes it a region of high negative vertical vorticity with the consequence that both top and bottom Ekman layers extract fluid. While the lower flux feeds the inward radial flow in the bottom Ekman layer, the upper $E^{1/4}$ layer flux adds to the outward flux of the upper Ekman layer which must "turn" the corner where the boundary velocity discontinuity occurs and flow down the side wall. A detailed analysis by Bisshop (1966) shows that this singular $E^{1/4} \times E^{1/2}$ corner region acts as the flux source for the $E^{1/3}$ layer which then carries the flux down the wall and feeds it uniformally into the $E^{1/4}$ layer.

Case 2: $\tan \alpha < E^{1/2}$:

The interior dynamics remain geostrophic when the bottom slope is increased from 0. Since the Proudman-Taylor theorem

holds to 0(E) and a vertical fluid column retains its form and moves without stretching or contraction, the interior vertical velocities (7) and (8) outside the two Ekman layers must again match.

Equating terms forms a steady vorticity equation,

$$\hat{k} \cdot \nabla \times \vec{u} + \frac{\tan \alpha}{E^{1/2}} \hat{j} \cdot \vec{u} = 1 \qquad (13)$$

which can be rewritten, using the pressure field, as

$$\nabla_2^2 p + \frac{\tan \alpha}{E^{1/2}} p_x = 2 \qquad (14)$$

The boundary condition on the inviscid interior flow is no-normal flux at $\lambda = a$, so

$$p(a, \theta) = C = 0$$

(the choice of the constant of integration $C = 0$ will be explained later). We now note that the parameter $\tan \alpha / E^{1/2}$ will determine the symmetry of the pressure field. For sufficiently small slopes that $\tan \alpha < E^{1/2}$, the pressure field will be almost parabolic, while for larger slopes a quite asymmetrical pressure field should result.

When $\tan \alpha < E^{1/2}$, the interior pressure field can be found using a regular perturbation expansion

$$p = \sum_{m=0} \left(\frac{\tan \alpha}{E^{1/2}} \right)^m p_m (\lambda, \theta)$$

The problem sequence for the unknown functions $[p_m]$ becomes

$$m = 0 \quad \nabla_2^2 p_0 = 2 \qquad p_0 (a, \theta) = 0$$

$$m \neq 0 \quad \nabla_2^2 p_m = -p_{m-1 K} \quad p_m (a, \theta) = 0$$

where p_0 is the parabolic field found in case 1 for $\alpha = 0$. The resulting perturbed pressure field is

$$p = \frac{\lambda^2 - a^2}{2} + \frac{\tan \alpha}{E^{1/2}} \left(\frac{a^2 \lambda - \lambda^3}{8} \right) \cos \theta + \dots$$

with velocity components

$$u = \qquad\qquad \frac{\tan \alpha}{E^{1/2}} \left(\frac{a^2 - \lambda^2}{16} \right) \sin \theta + \dots \qquad (15a)$$

$$v = \lambda/2 \quad + \quad \frac{\tan \alpha}{E^{1/2}} \left(\frac{a^2 - 3\lambda^2}{16} \right) \cos \theta + \dots \qquad (15b)$$

Akthough $u(a, \theta)$ vanishes, the interior tangential flow just outside the side wall boundary layer is clearly dependent on θ.

We need to examine the side boundary layer flow to see if this dependency changes the basic $E^{1/4}$, $E^{1/3}$ boundary layer structure.

We shall assume that $\tan \alpha = \Delta E^{3/4}$ where $0(\Delta) \sim 1$, and look at the $E^{1/4}$ layer structure dependence on Δ. The $\underline{correction}$ velocity and pressure fields in the $E^{1/4}$ layer can be expanded

$$u = \qquad\qquad E^{1/2} u_2 + \cdots$$
$$v = v_0 \quad + \quad E^{1/4} v_1 + \cdots$$
$$w = \qquad\qquad E^{1/4} w_1 + \cdots$$
$$p = \qquad\qquad E^{1/4} p_1 + \cdots$$

where each variable is further decomposed

$$f_i = f_{i0} + \Delta f_{i1}$$

The boundary layer thickness is also perturbed in Poincare's method

$$\frac{\partial}{\partial n} = - E^{1/4} \lambda \frac{\partial}{\partial s}$$
$$\lambda = 1 + E^{1/4}(\lambda_{10} + \Delta \lambda_{11}) + \cdots$$

Substituting these expansions into the basic equations and equating coefficients of like powers of $E^{1/4}$ yield the following balances

$$\hat{n}: \quad -2v_0 = p_{1s}$$
$$\qquad -2v_1 = p_{2s} + \lambda_1 p_{1s}$$
$$\qquad -2v_2 = p_{3s} + \lambda_1 p_{2s} + \lambda_2 p_{1s}$$

$$\hat{\theta}: \quad 0 = p_{1\theta}$$
$$\qquad 2u_2 = -\frac{1}{a} p_{2\theta} + v_{0ss}$$
$$\qquad 2u_3 = -\frac{1}{a} p_{3\theta} - s \frac{p_{2\theta}}{a^2} + v_{1ss} + 2\lambda_1 v_{0ss} - \frac{v_{0s}}{a}$$

$$\hat{k}: \quad p_{1z} = p_{2z} = 0$$

$$\text{Continuity} \qquad v_{0\theta} = 0$$
$$\qquad -u_{2s} + \frac{v_{1\theta}}{a} + w_{1z} = 0$$
$$\qquad -u_{3s} - \lambda_1 u_{2s} + \frac{u_2}{a} + \frac{v_{2\theta}}{a} + s\frac{v_{1\theta}}{a^2} + w_{2z} = 0$$

$$(16)$$

The pertinent boundary conditions at the Ekman layers are

$$\omega_1\left(s, \frac{1}{2} \pm \frac{1}{2}\right) = \pm \frac{v_{0s}}{2}$$

$$\omega_2\left(s, \frac{1}{2} \pm \frac{1}{2}\right) = \pm\left(\frac{v_{1s}}{2} + \lambda_1 \frac{v_{0s}}{2}\right)$$

and on the side wall,

$$\overline{v_0}\left(0, \theta, z\right) + v_{0in} = 0$$

$$v_1\left(0, \theta, z\right) + v_{1in} = 0$$

Since from (15b)

$$v_{in} = \frac{a}{2} - \frac{E^{1/4}\Delta a^2 \cos\theta}{8} +$$

the side wall condition becomes

$$v_0\left(0, \theta, z\right) = -\frac{a}{2}$$

$$v_1\left(0, \theta, z\right) = \frac{\Delta a^2}{8} \cos\theta$$

Solving the vertically integrated continuity equation to $0(E^{1/4})$ in terms of v_0 yields a governing equation for v_0

$$-\frac{v_{0sss}}{2} + v_{0s} = -\frac{v_0}{a}\frac{d\lambda_1}{d\theta}$$

Since both v_{0in} and therefore its correction field v_0 are independent of θ, and λ_1 must be periodic in θ, λ_1 must be a constant λ_1^*.

The governing equation for the next order v_1 is found in the same manner to be

$$-\frac{v_{1sss}}{2} + v_{1s} = \lambda_1^*\left\{\frac{3 v_{0sss}}{2} - v_{0s}\right\} - \frac{v_{0ss}}{a^2}$$

The solution for v_1 will contain secular terms of the form $s e^{-\sqrt{2}s}$ unless $\lambda_{10}^* = -\frac{1}{a\sqrt{2}}$ and $\lambda_{11}^* = 0$, so

$$v_{11} = \frac{\Delta a^2}{8} \cos\theta \, e^{-\sqrt{2}s} \qquad v_{10} = 0$$

The radial thickness of the $E^{1/4}$ layer is then to second order <u>independent</u> of the small bottom slope.

The lowest order $\hat{\theta}$-momentum balance is dependent on Δ, though, for

$$2\left(u_{20} + \Delta u_{21}\right) = -\frac{1}{a}\Delta p_{21\theta} + v_{0ss}$$

For $\Delta < 1$, the basic balance is ageostrophic between the Coriolis

force and shearing stress, similar to case 1. But for larger
slopes, $\Delta > 1$, the basic balance becomes <u>geostrophic</u>, with

$$2u_{2l} = -\frac{1}{a} p_{2l\theta} + O\left(\frac{1}{\Delta}\right)$$

Thus, the $O(\Delta E^{1/4})$ pressure field in dynamic balance with the
$O(\Delta E^{1/4})$ asymmetric azimuthal flow drives a geostrophic radial
flow of $O(\Delta E^{1/2})$ and form.

$$u_{2l} = \frac{a}{8\sqrt{2}} \Delta m \theta \, e^{-\sqrt{2}S}$$

This flow must be fed by either the interior or $E^{1/3}$ layer.

To determine the flux source, suppose that the total radial
velocity u is decomposed into the interior and the two boundary
layer <u>correction</u> components,

$$u = u_{in} + \tilde{u}_{1/4} + \tilde{u}_{1/3}$$

where by the no-normal flux boundary condition

$$\langle u \rangle = \frac{1}{2\pi} \int_0^{2\pi} u(a, z, \theta') \, d\theta' = \langle u_{in} \rangle + \langle \tilde{u}_{1/4} \rangle + \langle \tilde{u}_{1/3} \rangle = 0$$

Since the interior is always geostrophic and the $E^{1/3}$ layer is not,

$$\langle u_{in} \rangle = 0 \quad , \quad \langle \tilde{u}_{1/3} \rangle \neq 0$$

For $\Delta < 1$, the basic $\hat{\theta}$-momentum balance in the $E^{1/4}$ layer is
ageostrophic so that the basic balance

$$\langle \tilde{u}_{1/4} \rangle + \langle \tilde{u}_{1/3} \rangle = 0$$

occurs. But when $\Delta > 1$, that balance in the $E^{1/4}$ layer becomes
geostrophic with the result that to lowest order, $\langle \tilde{u}_{1/4} \rangle = 0$.
Since this implies $\langle \tilde{u}_{1/3} \rangle = 0$ to $O(\Delta E^{1/4})$, the $O(\Delta E^{1/2})$ radial
flow in the $E^{1/4}$ layer cannot be supplied from the $E^{1/3}$ layer but
must feed the geostrophic interior. This means that the
$O\left(\frac{\tan\alpha}{E^{1/2}}\right)$ interior asymmetric flow is modified by the $E^{1/4}$ layer
with $E^{1/2}$ an $O\left(\frac{\tan\alpha}{E^{1/4}}\right)$ radial flow, while both the $E^{1/4}$ layer scale
thickness and the $E^{1/3}$ layer flow and dynamics are not modified
to lowest order.

Case 3: $E^{1/2} < \tan\alpha < E^{1/4}$

The previous perturbation scheme breaks down for larger
slopes. However, a general analytic solution for the pressure

field exists and may be found directly. After the particular solution to (14) is found with $p_p = \frac{2E^{1/2}x}{\tan\alpha}$, the homogeneous problem can be reduced to a Helmholtz equation

$$\nabla_2^2 f - \left(\frac{\tan\alpha}{2E^{1/2}}\right)^2 f = 0$$

by the substitution

$$p_h = e^{-\frac{\tan\alpha \, x}{2E^{1/2}}} f(x,y)$$

Adding homogeneous and particular solutions gives for the general pressure solution

$$\frac{p}{a^2} = \frac{x'}{\Gamma} + e^{-\Gamma x'}\left\{\sum_{m=0} I_m(\Gamma r')\left(C_1(m)\sin m\theta + C_2(m)\cos m\theta\right)\right\}$$

where $\Gamma = \frac{\tan\alpha}{2E^{1/2}}a$ and x' and r' are normalized by the non-dimensional radius a. The appropriate boundary condition is still $p(a,\theta) = C$ to $O(E^{1/4})$ so that the unknown fourier coefficients may be found in the usual way by series evaluation on the boundary

$$\sum_{m=0} I_m(\Gamma)\left\{C_1(m)\sin m\theta + C_2(m)\cos m\theta\right\} = \frac{\cos\theta}{\Gamma}e^{\Gamma\cos\theta} + Ce^{\Gamma\cos\theta}$$

The particular choice C = 0 simplifies the computation, giving for the interior geostrophic pressure field

$$\frac{p}{a^2} = \frac{1}{\Gamma}\left\{r'\cos\theta - e^{-\Gamma r'\cos\theta}\left\{\frac{I_1(\Gamma)}{I_0(\Gamma)}I_0(\Gamma r') + \sum_{m=1}^{\infty}\frac{I_{m+1}(\Gamma)+I_{m-1}(\Gamma)}{I_m(\Gamma)}I_m(\Gamma r')\cos m\theta\right\}\right\} \quad (17)$$

This series converges for all finite Γ and has been evaluated numerically by computer for several values of Γ . The streamlines are shown in Fig. 2. (Discussion of the numerical solution method is given in Appendix A).

The pressure field is an even function of θ but not of x. Fig. 3 is a plot of $p_{a^2}(r,\theta)$ along the x-axis, showing a shift of the circulation center where $p_x = 0$ from the origin westward to x -.25 for $\Gamma = 1$. This shift is more pronounced for larger values of Γ . The degree of asymmetry of the pressure field or streamlines clearly depends on the value of Γ . For the streamlines of two different basins to be geometrically similar the

shallow

π ─| |─ O

deep

a) $\Gamma = 0.2$

shallow

π ─| |─ O

deep

b) $\Gamma = 1.0$
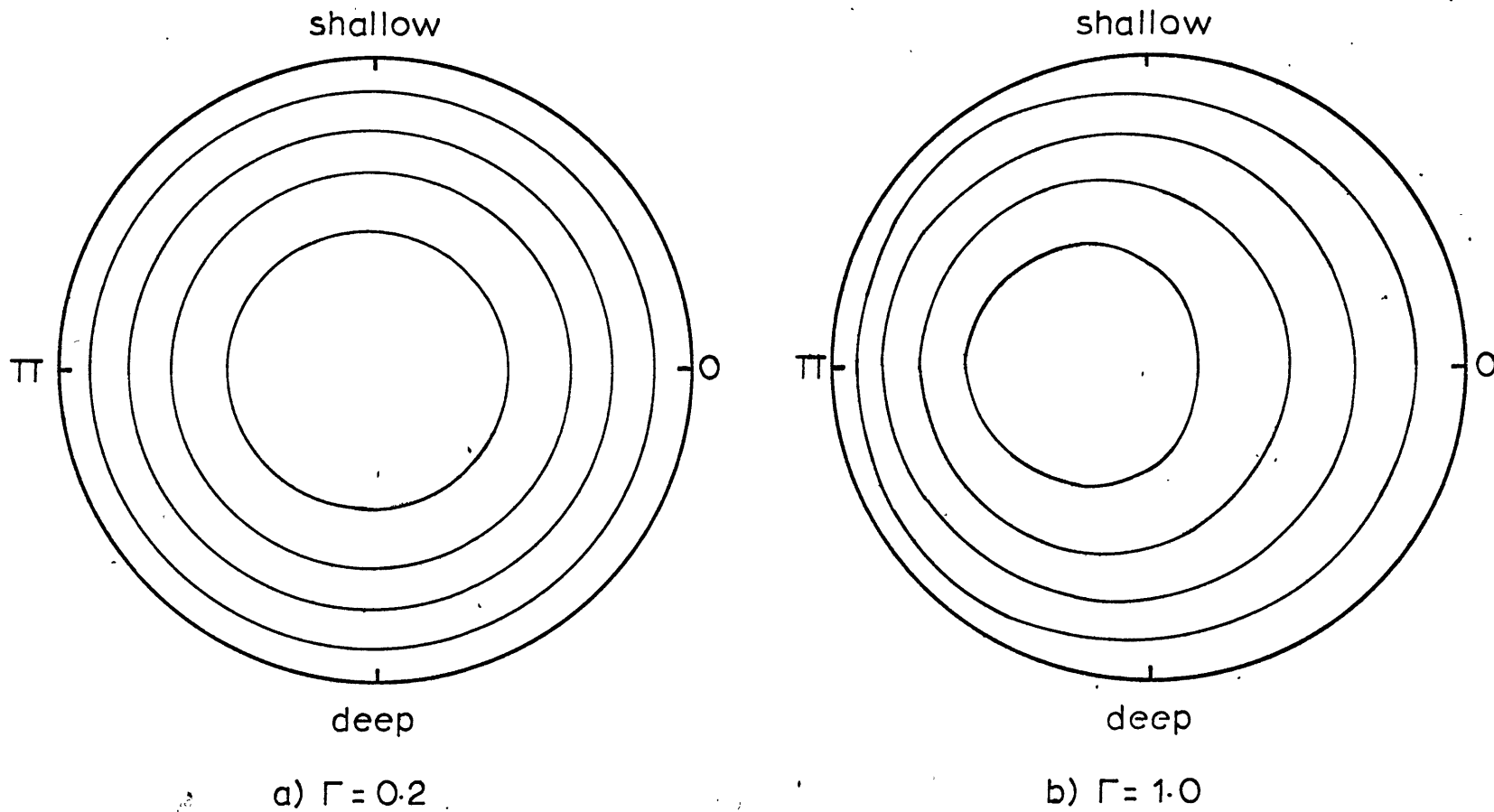
FIGURE 2. Interior pressure isobars as a function of Γ.

shallow

π — — O

deep

c) Γ = 2·0

shallow

π — — O

deep
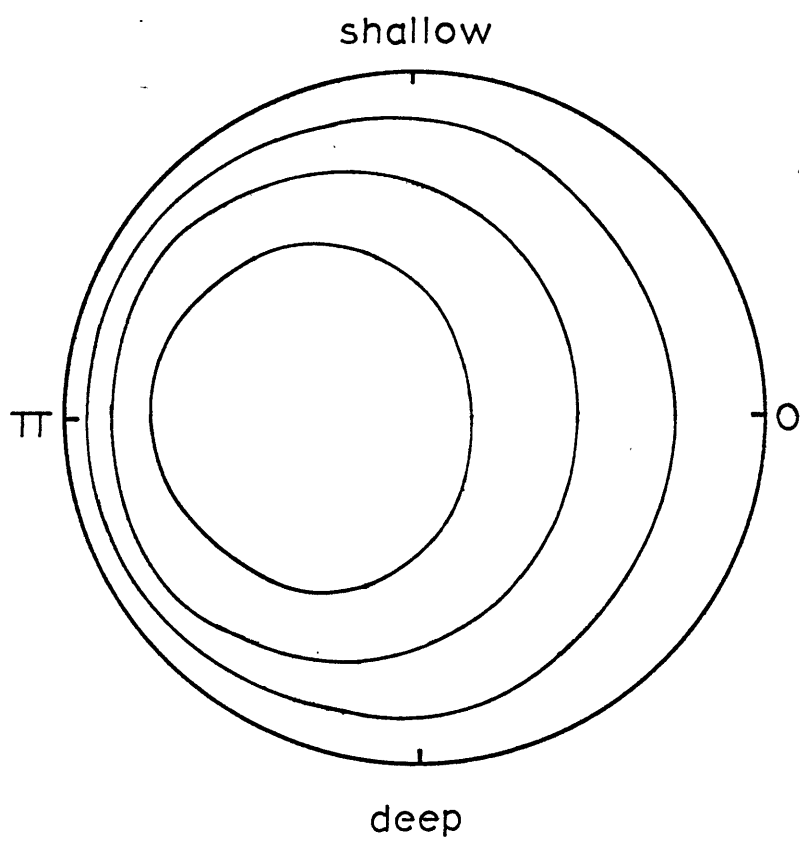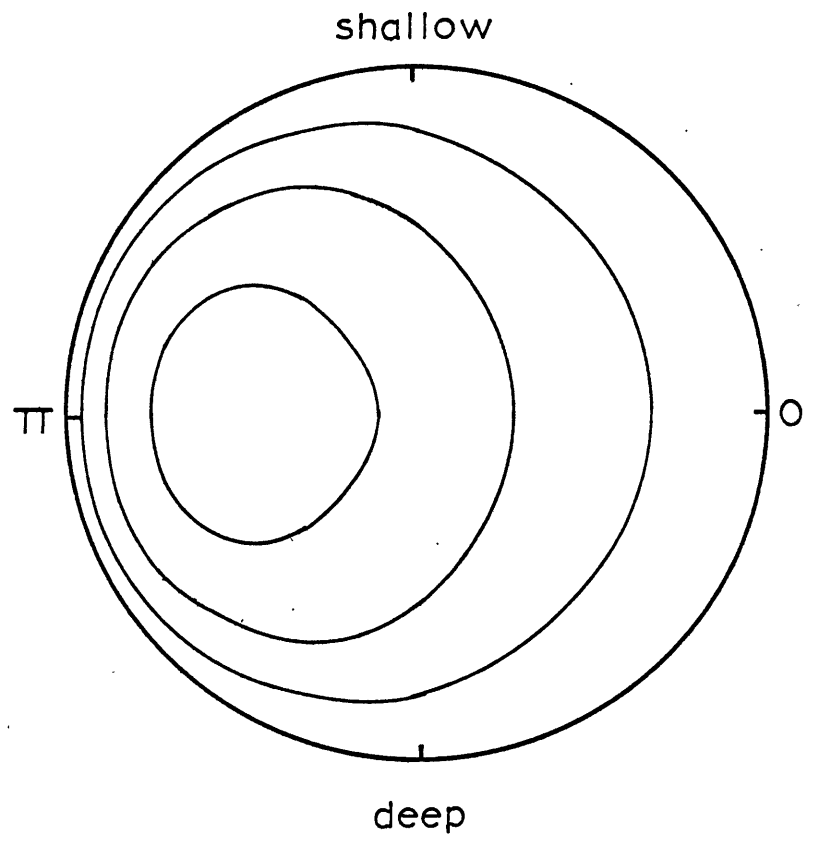
d) Γ = 3·0

FIGURE 2 (con't).

FIGURE 3. Interior pressure field along E - W axis versus Γ.

value of Γ must be identical. Since Γ is proportional to the ratio of total depth variation to the Ekman layer thickness, twice the bottom slope is needed for a basin with half the original diameter.

For $\Gamma \gtrsim 3$, the intense crowding of streamlines along the $3\pi/2 < \theta < \pi/2$ boundary slow the development of a geostrophic boundary layer. In analogy to the β-plane wind-driven ocean circulation models, we will call this layer the western boundary layer.

The structure of this geostrophic layer may be easily found using the regular perturbation expansion

$$p = \sum_{m=1} \left(\frac{E^{1/2}}{\tan\alpha}\right)^m \left(p_m(r,\theta) + \tilde{p}_m(\rho,\theta)\right)$$

with the tilde indicating a boundary layer correction field and ρ, and appropriate stretched coordinate defined by

$$(a-r) = \frac{E^{1/2}}{\tan\alpha} \rho$$

The vorticity equation expressed in cylindrical coordinates shows that basic dynamic balances are

$$p_{1x} = 2 \tag{18}$$

which is again the Sverdrup balance in the interior and

$$\tilde{p}_{1\rho\rho} - \cos\theta \; \tilde{p}_{1\rho} = 0$$

in the boundary layer. Its solution

$$\tilde{p}_1 = A(\theta) + B(\theta)e^{\cos\theta\,\rho}$$
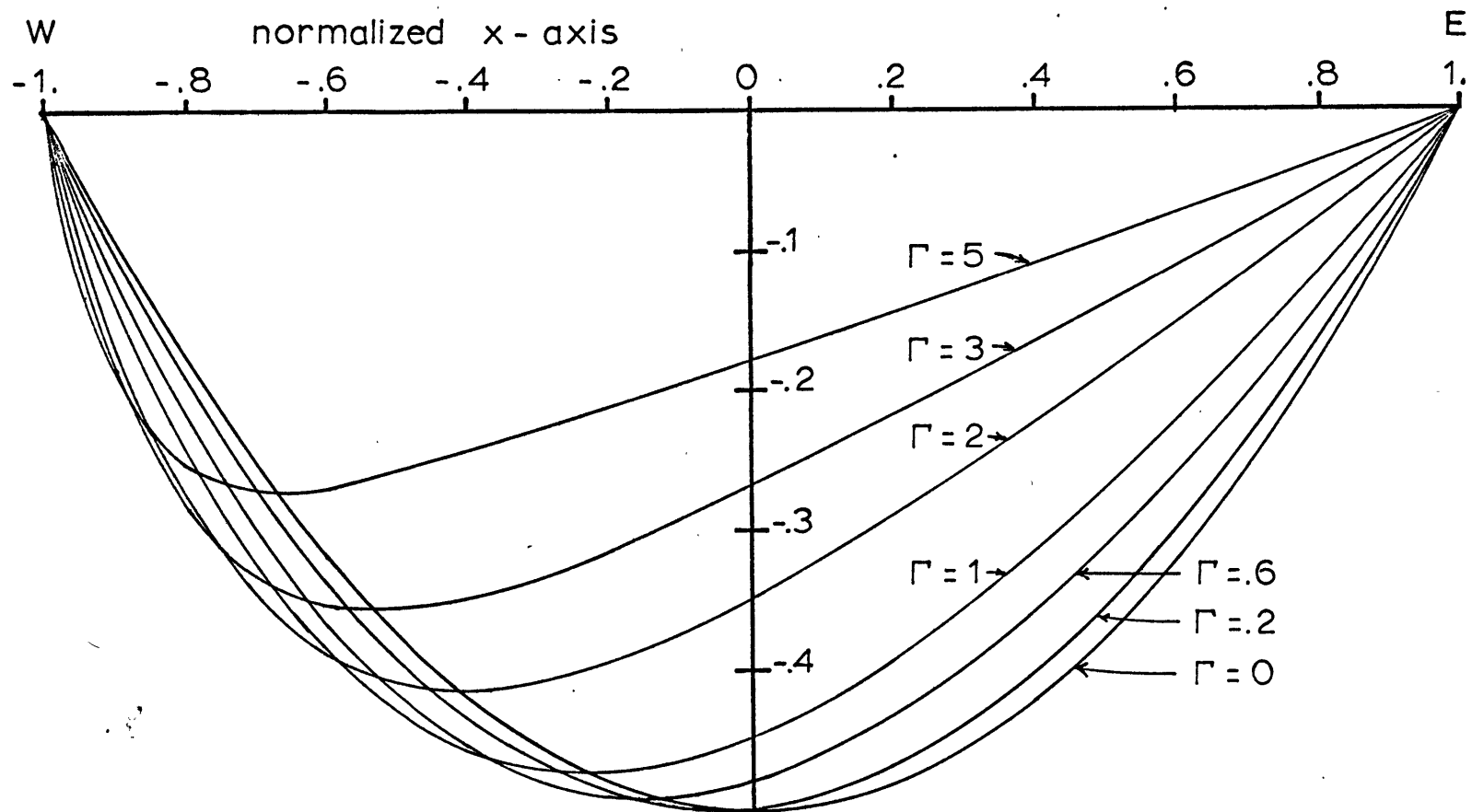
decays properly into the interior when $\cos\theta < 0$, i.e., along the western side only. The boundary condition on the interior solution along the eastern boundary is then no-normal flux. This specifies the component of flow parallel to the basin depth contours in terms of the cross-contour component given by the Sverdrup balance, thus determining the unknown function $f(y)$ in the interior solution to (18)

$$p_1 = 2(x + f(y))$$

to be

$$f(y) = - \sqrt{a^2 - y^2} \qquad (19)$$

This is identical to Pedlosky and Greenspan's interior results. The interior streamlines are circular arcs, closing in the western boundary layer. There, the pressure field is found by matching radial fluxes to be

$$p = 4a \cos\theta \left(1 - e^{\cos\theta \varsigma}\right)$$

These solutions indicate a new interior scale of motion. For $\tan\alpha \gtrsim E^{1/2}$, the bottom slope constrains the interior flow to be $O\left(E^{1/2}/\tan\alpha\right)$ while in the western boundary current $O(v) \sim$ flux/thickness ~ 1. As $\tan\alpha$ increases toward $E^{1/4}$, the geostrophic boundary layer thickness decreases toward the $E^{1/4}$ layer scale and the interior flow decreases toward $O(E^{1/4})$, the magnitude of the forced radial motion from the lowest order geostrophic balance in the $E^{1/4}$ layer. We will see next that the $E^{1/4}$ boundary layer structure undergoes a change when $\tan\alpha \rightarrow E^{1/4}$.

Case 4: $E^{1/4} \lesssim \tan\alpha < E^{1/6}$:

We will now look at the E layer along the western boundary. Let $\tan\alpha = \Delta E^{1/4}$ with Δ again assumed to be $O(1)$. The complete velocity and pressure field equations in the $E^{1/4}$ layer are

$$v = v_0 + E^{1/4} v_1$$
$$u = E^{1/4} u_1 + E^{1/2} u_2 \ldots$$
$$w = E^{1/4} w_1 + \ldots$$
$$p = p_0 + E^{1/4} p_1 + \ldots$$

and ς is again the stretched boundary layer coordinate. The dominant boundary layer balances are

$$\hat{r}: \quad 2v_0 = -p_{1\varsigma}$$
$$\phantom{\hat{r}:\quad} 2v_1 = -p_{2\varsigma}$$
$$\hat{\theta}: \quad 2u_1 = -p_{1\theta}$$
$$\phantom{\hat{\theta}:\quad} 2u_2 = -\frac{p_{1\theta}}{a} - \frac{\varsigma p_{1\theta}}{a^2} + v_{0\varsigma\varsigma}$$
$$\hat{k}: \quad p_{1z} + p_{2z} = 0$$

continuity: $\quad -u_{1\varsigma} + \frac{v_{0\theta}}{a} = 0$
$$-u_{2\varsigma} + \frac{u_1}{a} + \frac{v_{1\theta}}{a} + \frac{v_{0\theta}\varsigma}{a^2} + w_{1z} = 0$$

The Ekman layer fluxes are

$$w_1 = \frac{v_{03}}{2} \quad \text{at} \quad z = 1$$

$$w_2 = -\frac{v_{03}}{2} + \Delta \cos\theta \, v_0 \quad \text{at} \quad z = \tan\alpha \; a \sin\theta$$

With $\tan\alpha$ approaching $E^{1/4}$, the bottom slope is sufficiently
large that the orographic component becomes comparable to the
Ekman layer suction. This modifies the governing equation for
v_0, found in the same manner as before, to

$$v_{0SSS} - 2v_{03} + 2\Delta \cos\theta \, v_0 = 0$$

where the lateral diffusion of vorticity from the side boundary
is now balanced by Ekman layer and orographic vortex stretching.
For eigenfunctions of the form $A_i(\theta) \, e^{\lambda_i(\theta)S}$, the eigenvalue
equation reduces to the cubic

$$\lambda_i^3 - 2\lambda_i + 2\Delta\cos\theta = 0$$

Since our scaling is valid only along the western boundary,
$\Delta\cos\theta$ can be replaced by $-\Box$ where $\Box = |\Delta\cos\theta|$. The
eigenvalues for $\Delta < \left(\frac{2}{3}\right)^{\frac{3}{2}}$ are

$$\lambda_1 = 2\sqrt{2/3} \, \cos(\phi/3)$$

$$\lambda_2 = 2\sqrt{2/3} \, \cos(\phi/3 + 2\pi/3)$$

$$\lambda_3 = 2\sqrt{2/3} \, \cos(\phi/3 - 2\pi/3)$$

with $\tan\phi = \dfrac{\sqrt{(2/3)^3 - \Delta^2\cos^2\theta}}{|\Delta\cos\theta|} = \dfrac{\sqrt{(2/3)^3 - \Box^2}}{\Box}$

When $\Delta \ll 1$, ϕ approaches $\pi/2$ and these roots may be expanded to

$$\lambda_1 = \sqrt{2} + \frac{\Box}{2} + \cdots$$

$$\lambda_2 = -\sqrt{2} + \frac{\Box}{2} + \cdots$$

$$\lambda_3 = \qquad - \Box + \cdots$$

The usable roots must have a negative real value for exponential

decay into the interior so λ_1 is excluded. λ_2 corresponds to a thickening of the standard $E^{1/4}$ layer towards $\theta = \pi$ while λ_3 corresponds to the interior geostrophic boundary layer. The azimuthal flow in the $E^{1/4}$ layer is then

$$v_0 = A_2(\theta)\left(e^{\lambda_2 s} - e^{\lambda_3 s}\right)$$

The pressure field is found by integrating the geostrophic balance

$$p_1 = p_{10} + \int_0^s -2v_0 \, ds' = p_{10} - 2A_2\left\{\frac{e^{\lambda_2 s}-1}{\lambda_2} - \frac{e^{\lambda_3 s}-1}{\lambda_3}\right\}$$

Since the lowest order momentum balance in the western $E^{1/4}$ layer is geostrophic, the appropriate boundary condition on p_1 is again $p_{1\theta}(0,\theta) = 0$. Since the eastern boundary is a streamline with $p_{in} = 0$, the western boundary must be a streamline with $p(0,\theta) = 0$, so the integration constant $p_{10} = 0$. We can now match p_1 with the interior pressure field on the western boundary to determine A_2:

$$\lim_{s \to \infty} p_1 = 2A_2(\theta)\left(\frac{1}{\lambda_2} - \frac{1}{\lambda_3}\right) = \lim_{\eta \to a} p_{?u} = \frac{4a\cos\theta}{\Delta}$$

For $\Delta \ll 1$, $\lambda_3 < \lambda_2$ so the basic balance is

$$-\frac{2A_2}{\lambda_3} = \frac{4a\cos\theta}{\Delta}$$

which illustrates the basic role of the interior geostrophic boundary layer in closing the north-south horizontal circulation when $\tan\alpha < E^{1/4}$. With $\lambda_3 \sim -\Delta|\cos\theta|$, $A_2 = -2a\cos^2\theta$ and the azimuthal flow in the $E^{1/4}$ layer is

$$v_0 = 2a\cos^2\theta\left\{e^{-|\Delta\cos\theta|s} - e^{-\left(\sqrt{2} - \frac{\Delta|\cos\theta|}{2}\right)s}\right\}$$

As $\tan\alpha$ increases toward $E^{1/4}$, the interior and $E^{1/4}$ boundary layers tend to merge until $\lambda_2 = \lambda_3$ at $\theta = \pi$ for $\tan\alpha = \left(2/3\right)^{3/2} E^{1/4}$

For greater slopes, the two roots become complex conjugates

$$\lambda_2 = -a + b\, e^{\frac{2\pi i}{3}}$$

$$\lambda_3 = -a + b\, e^{-\frac{2\pi i}{3}}$$

with $a = \left(\square - \sqrt{\square^2 - (2/3)^3} \right)^{1/2}$

$\qquad b = \left(\square + \sqrt{\square^2 - (2/3)^3} \right)^{1/2}$

along an arc centered about $\theta = \pi$. The transition point between λ_2, λ_3 real and complex is θ_c where $\cos^2\theta_c = 8\,E^{1/2}/27\tan^2\alpha$. For $\tan\alpha \gg E^{1/4}$, the endpoints of the arc rapidly approach $\pi/2$ and $3\pi/2$, while $a \to 0$, $b \to \sqrt[3]{2\square}$. Along this arc, A_2 is given by the new balance

$$2A_2\left\{ \frac{1}{\lambda_2} - \frac{1}{\lambda_2^*} \right\} = \frac{4a\cos\theta}{\Delta}$$

with $\quad \dfrac{1}{\lambda_2} - \dfrac{1}{\lambda_2^*} = -\sqrt{3}\,i\,(2\square)^{-1/3} + O(1/\square)$

The resulting western $E^{1/4}$ boundary layer flow is

$$v_0 = \frac{4\sqrt[3]{2}}{\sqrt{3}} \frac{a|\cos\theta|^{4/3}}{\Delta^{2/3}} e^{-\frac{\tilde{\gamma}s}{2}} \sin \frac{\sqrt{3}}{2}\tilde{\gamma}s \qquad (20)$$

where $\quad \tilde{\gamma} = \sqrt[3]{2\Delta|\cos\theta|}$

As $\tan\alpha$ increases from $E^{1/4}$, the modified western $E^{1/4}$ layer ($mE^{1/4}$) becomes thinner and sweeps toward the side wall. The result of Pedlosky and Greenspan (1967) is re-obtained when (20) is rewritten in terms of $\tan\alpha$ and E,

$$v_0 = \frac{4\sqrt[3]{2}}{\sqrt{3}} \frac{a|\cos\theta|^{4/3}}{(\tan\alpha)^{2/3}} E^{1/6} e^{-\frac{\gamma(a-r)}{2E^{1/3}}} \sin\left\{ \frac{\sqrt{3}}{2}\frac{\gamma(a-r)}{E^{1/3}} \right\} \quad (21)$$

with $\quad \gamma = \sqrt[3]{2\tan\alpha\,|\cos\theta|}$

Even though the analysis by Pedlosky and Greenspan of the western boundary layer as a $E^{1/3}$ layer is valid in a strict sense only for $\tan\alpha > E^{1/6}$, the solution also illustrates the fundamental nature of the western boundary layer for the larger range of $\tan\alpha > E^{1/4}$. The dynamics for this are now clearer. The horizontal momentum balances in the $mE^{1/4}$ layer are essentially geostrophic in both $\hat{r}$- and $\hat{\theta}$-components while the pressure field is independent of z to lowest order. As $\tan\alpha$ increases from $O(E^{1/4})$, the $mE^{1/4}$ layer -- normally two-dimensional and now geostrophic --

shrinks in thickness to become the modified $E^{1/3}$ layer that was found by Pedlosky and Greenspan. The key to the boundary layer thinning lies, of course, in the $E^{1/4}$ layer vertical vorticity balance. For $\tan \alpha < E^{1/4}$, the lateral viscous diffusion of negative vorticity from the side wall is balanced primarily by positive vortex stretching by both Ekman layers. Increasing the bottom slope increases the orographic component of this stretching until it dominates the Ekman suction component. Any further increase in the orographic component by increasing the bottom slope must be balanced by an increased lateral viscous vorticity flux, hence a higher velocity shear and a smaller boundary layer thickness.

Case 5 : $E^{1/6} < \tan \alpha < 1$:

At this point, the role of the $E^{1/3}$ layer should be reconsidered. For $\tan \alpha < E^{1/2}$ we have seen that the $E^{1/3}$ layer carries the radial outflux from the top Ekman layer down the side wall and feeds it uniformally into the $E^{1/4}$ layer, which redistributes this radial flux back into both Ekman layers. A moderate slope, however, constrains the vertical outflux from the bottom Ekman layer to be of $O(E^{1/2}/\tan \alpha)$ so the bottom Ekman layer can __not__ close the $O(E^{1/2})$ vertical secondary circulation. Instead, the $E^{1/3}$ layer outflux must feed the interior and western boundary layer directly.

To illustrate this transition, we will now assume that $E^{1/6} << \tan \alpha < 1$ and proceed with Pedlosky and Greenspan's analysis. The basic non-dimensional boundary layer equations for the correction fields are in component form

$$- 2V = P_\eta$$

$$2U = -\frac{P_\theta}{a} + V_{\eta\eta}$$

$$0 = -P_z + W_{\eta\eta}$$

$$-U_\eta + \frac{U_\theta}{a} + W_z = 0$$

where the variables have been scaled according to

$$u = E^{1/2} U$$
$$V = E^{1/6} V$$
$$w = E^{1/6} W$$

$$p = E^{1/2} P$$
$$\frac{\partial}{\partial r} = -\frac{1}{E^{1/3}} \frac{\partial}{\partial \eta}$$

The momentum equations can be eliminated to yield a single governing equation for the pressure function,

$$P_{\eta\eta\eta\eta} + 4P_{zz} = 0 \qquad\qquad (21)$$

with the appropriate boundary conditions being

$$P_z = 0 \qquad\qquad at \quad z = 1$$
$$P_z = -\frac{1}{2} \tan\alpha \cos\theta \, P_{\eta\eta} \qquad at \quad z = \tan\alpha \, a \sin\theta$$

and on the side wall

$$P_\eta = P_{\eta\eta\eta} = 0 \qquad\qquad (22a)$$
$$\frac{1}{2a} P_\theta + \frac{1}{4} P_{\eta\eta} = U^* \qquad\qquad (22b)$$

At this point, Pedlosky and Greenspan set U^* equal to the $O(E^{1/2}/\tan\alpha)$ interior radial flux to obtain the first order pressure solution. We will find the pressure field to second order in $\tan\alpha$ by setting U^* equal to the combined $O(E^{1/2}/\tan\alpha)$ and $O(E^{1/2})$ radial flux from the interior and the thinner normal E layer.

(21) may be solved with eigenfunctions of the form

$$P = \sum_n A_n e^{-\lambda_n \eta} \cos\left[\frac{1}{2}\lambda_n^3(1-z)\right]$$

provided λ_n satisfies

$$\tan\frac{1}{2}\lambda_n^3 (1 - a\tan\alpha\sin\theta) = \tan\alpha\cos\theta$$

Pedlosky and Greenspan have shown that the eigenroots compose two sets, one of three complex roots of $O(\tan\alpha^{1/3})$ associated with the western modified $E^{1/3}$ layer and the countable set of $O(1)$ complex roots associated with the normal $E^{1/3}$ layer.

Expansion of the eigenvalue equation in powers of $\tan\alpha$ shows that the two smaller roots which give exponential decay into the interior from the western boundary are to second order

$$(\lambda_2, \lambda_3) = |2\tan\alpha \cos\theta|^{1/3} \left\{ 1 + \frac{a\tan\alpha \sin\theta}{3} \right\} (e^{\frac{\pi}{3}i}, e^{-\frac{\pi}{3}i})$$

The general pressure function satisfying the no-slip sidewall conditions (22a,b) is then

$$P = A \left(e^{-\lambda_2 \eta} e^{-\frac{\pi}{3}i} - e^{-\lambda_3 \eta} e^{\frac{\pi}{3}i} \right)$$

where the $O(\tan^2\alpha)$ z-dependence is ignored. The amplitude A is found directly by matching the $mE^{1/3}$ radial flux with U^*, the combined interior and $nE^{1/3}$ layer fluxes.

Since the vertical flux into the upper Ekman layer is to lowest order independent of θ, the radial outflux from this layer is axisymmetric. The net radial velocity of the $nE^{1/3}$ layer is then, by continuity, $u = -aE^{1/2}/2$. Since the $mE^{1/3}$ layer exists on the western side only, the interior radial velocity must match the $nE^{1/3}$ layer flux along the eastern boundary. When evaluated in terms of the interior pressure function

$$p = \frac{2E^{1/2}}{\tan\alpha} \left(x - \chi^0(y) - \tan\alpha \, \chi'(y) \right)$$

This radial matching requires

$$\hat{n}\cdot\vec{u} \Big|_{\substack{\wedge=\frac{\alpha}{\cos\theta}>0}} = \frac{E^{1/2}}{\tan\alpha} \left\{ \sin\theta + (\cos\theta)\chi^0_y + \tan\alpha \cos\theta \, \chi'_y \right\} = -\frac{aE^{1/2}}{2}$$

The unknown functions χ^0, χ' associated with the interior flow parallel to the depth contours are found by equating powers of $\tan\alpha$ and solving, giving for the complete interior pressure

$$p = \frac{E^{1/2}}{\tan\alpha} \left(x - \sqrt{a^2 - y^2} + \frac{\tan\alpha \, a^2}{2} \sin^{-1}\left(\frac{y}{a}\right) \right)$$

Matching the interior and $nE^{1/3}$ layer radial fluxes along the western boundary to the $mE^{1/3}$ layer flux now reduces (22) to an ordinary differential equation for the unknown amplitude A,

$$-\frac{\sqrt{3}i}{2a} \left\{ \frac{d}{d\theta} - a\tan\alpha \cos\theta (1 + a\tan\alpha \sin\theta) \right\} A = \frac{2\sin\theta}{\tan\alpha} + a$$

The solution is found by expanding A in the series

$$\tan\alpha \, A = A^0 + \tan\alpha \, A' + \cdot \cdot \cdot \cdot$$

and solving the resulting perturbation equations

$$-\frac{\sqrt{3}\,i}{2a}\,\frac{dA^0}{d\theta} = 2\sin\theta \qquad\qquad A^0 = -\frac{4ai\cos\theta}{\sqrt{3}} + c^0$$

$$-\frac{\sqrt{3}\,i}{2a}\,\frac{dA'}{d\theta} + \frac{\sqrt{3}\,i}{2}\cos\theta\,A^0 = a \qquad A' = -\frac{a^2 i}{\sqrt{3}}\left\{\sin 2\theta - 2c^0\sin\theta + c'\right\}$$

Since the horizontal and vertical secondary flows are now matched to $O(E^{\frac{1}{2}})$ by radial boundary layer fluxes, continuity requires that no additional fluid enter or leave the $mE^{\frac{1}{3}}$ layer by a tangential flux where the layer terminates at $\theta = \pi/2$, $3\pi/2$. This implies that the pressure function must vanish at $\theta = \pi/2$ and $\theta = 3\pi/2$, indicating that the unknown constants of integration are both zero.

With the $mE^{\frac{1}{3}}$ layer pressure function found, the complete azimuthal boundary layer velocity may be given to $O(E^{\frac{1}{6}})$ by adding the $nE^{\frac{1}{3}}$ layer solution found in Section 1

$$v = \epsilon\Omega L E^{\frac{1}{6}}\left\{\sum_{m=1}^{\infty}\frac{2a}{\sqrt{3}}\frac{(-1)^m}{m\pi}\gamma_m\, e^{-\frac{\gamma_m \eta}{2}}\sin\frac{\sqrt{3}\,\gamma_m \eta}{2}\cos m\pi z \;+\right.$$

$$\left. |2\tan\alpha\cos\theta|^{\frac{1}{3}}\left\{\frac{-4a\cos\theta}{\tan\alpha\sqrt{3}} - \frac{a^2}{\sqrt{3}}\frac{5}{3}\sin 2\theta\right\}\sin\frac{\sqrt{3}}{2}\gamma\eta\, e^{-\frac{\gamma\eta}{2}}\right\} \qquad (23)$$

where the eigenroots are again

$$\gamma_m = (2m\pi)^{\frac{1}{3}}$$

$$\gamma = |2\tan\alpha\cos\theta|^{\frac{1}{3}}\left\{1 + \frac{\tan\alpha\, a\sin\theta}{3}\right\}$$

The vertical mass flux extracted from the interior by the upper Ekman layer is returned to the interior via the thinner axisymmetric $nE^{\frac{1}{3}}$ layer. The radial outflux from this layer along the eastern side is carried parallel to the geostrophic contours from east to west into the ageostrophic western $mE^{\frac{1}{3}}$ layer where it combines with the inner $nE^{\frac{1}{3}}$ layer outflux along the western boundary to produce a net convergence. Because of this convergence, the mass flux lost by the fluid column as it was carried through the interior region from deep to shallow end is restored as it returns to the deep end via the $mE^{\frac{1}{3}}$ layer.

The net convergence, coupled with the second order influence of the finite bottom slope on the $mE^{\frac{1}{3}}$ boundary layer thickness, distorts the first order north-south symmetry. According to (23), the position of the azimuthal velocity maximum is moved

through the angle $\Delta\theta = \sin^{-1}(5/8\alpha\tan\alpha)$ from the east-
west axis toward the shallow end. (23) is valid to $O(E^{1/6})$. The
$O(E^{1/3})$ contribution due to the inclusion of Ekman layers above
and below the $mE^{1/3}$ layer has not been determined, so the possible
discrepancy between (23) and the complete perturbation solution
is of $O(E^{1/6})$. The experiments were conducted over a range of E
such that $.147 < E^{1/6} < .198$, so the discrepancy might be appreciable,
especially when $\tan\alpha < E^{1/6}$. On the other hand, this theoretical analysis
suggests that the western $mE^{1/3}$ layer thickness dependence on E
is valid over a wider range of $\tan\alpha$ from $\tan\alpha > E^{1/4}$

3. Experimental Apparatus and Methods

3.1 Apparatus

The fluid container consisted of a lucite cylinder
with a $12.700\pm.005$ cm inner radius, capped at both ends by lucite
plates (see Fig. 4). The sliced cylinder geometry was formed by
inserting a false top and bottom into the cylinder. The geometry
shown in Fig. 4 has been inverted simply to ease construction.

Three lucite sloping bottoms were constructed from 0.92
cm thick plate stock for nominal angles of $\alpha \sim 6°$ ($\tan\alpha = .171\pm.003$),
$8°$ ($\tan\alpha = .144\pm.003$), and $10°$ ($\tan\alpha = .178\pm.003$). The actual
bottom slope was measured with a cathotometer while the false
bottoms were in place and the fluid container filled. The top
driving disk was a 0.61 cm thick glass plate of radius 12.675 cm.
Its plane of rotation was determined by the vertical positions of
three supporting miniature ball bearings since the glass disk was
optically flat and its surfaces parallel. The average separation
between the side wall and the false bottom, and the side wall and
the glass disk, was 0.025 cm, typically about 45% of the Ekman
layer scale thickness $LE^{1/2}$.

The glass disk was driven by a synchronous clock motor
using a shaft and gear train arrangement to help ensure a constant
relative angular velocity and thus a constant Rossby number. A
stable audio oscillator-amplifier system drove the motor so that
the relative angular velocity of the glass disk could be varied

35mm camera ⟶

sloping "bottom"

Cu-Con thermocouple

0.025 cm clearance

0.0025 cm diameter platinum wire

12.75 cm

miniature ball bearing

rotating glass disk

circular flourescent lamp

expansion clamp

sequence timer

clock motor

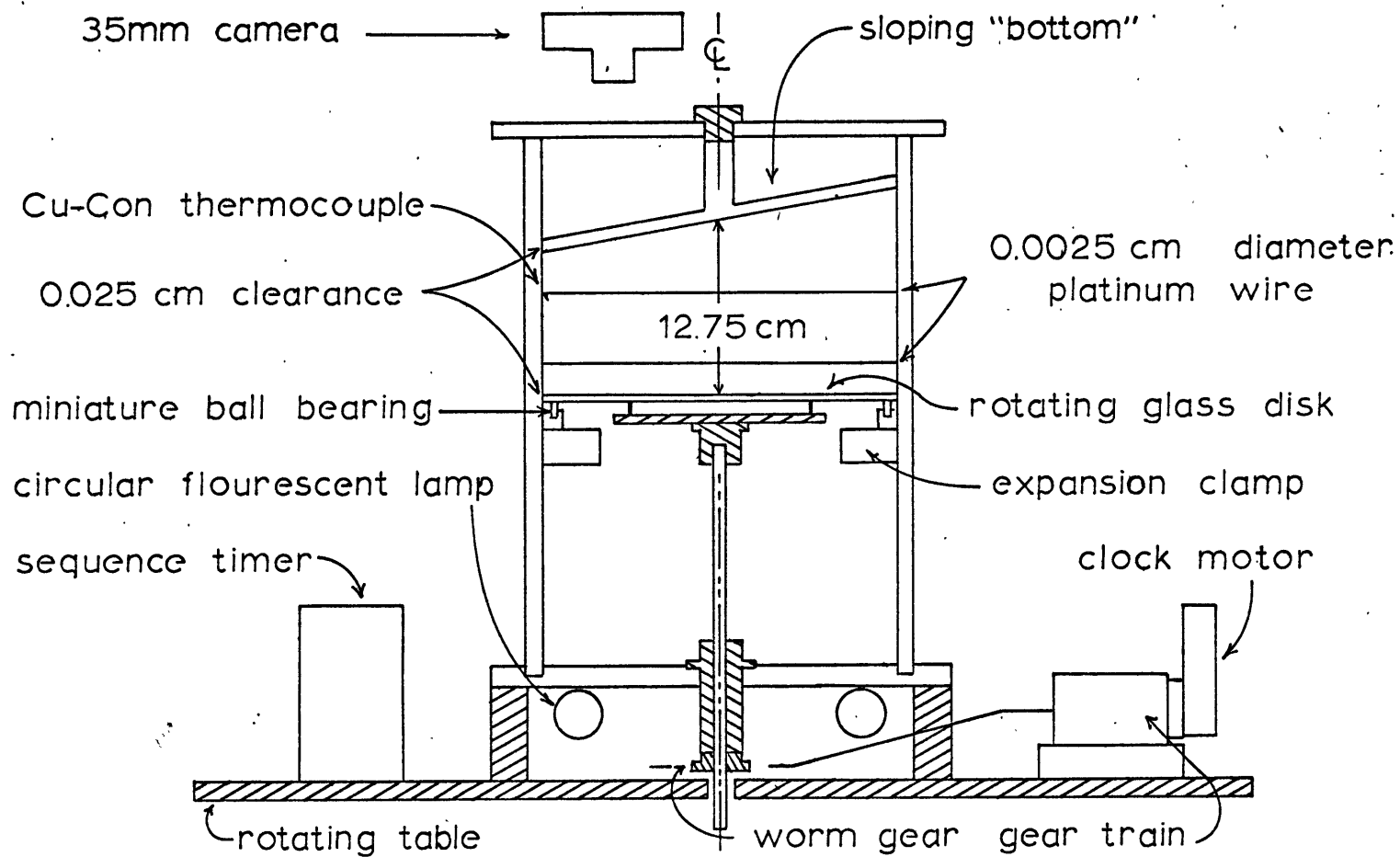rotating table

worm gear   gear train

FIGURE 4. Diagram of apparatus, side view (cross section)

by adjusting either the oscillator frequency or the gear reduction ratio. The apparatus was mounted on a rotating turntable driven by a synchronous motor through a direct drive Graham variable speed transmission. The relative angular velocity of the glass disk was quite constant, depending on the stability of the oscillator frequency. The angular velocity of the turntable was an order of magnitude less constant, being limited mainly by the stability of line frequency. Typical fractional standard deviations of f_{osc} and the turntable's rotation period were $< 2 \times 10^{-5}$ (100 cycles) and $< 2.10^{-4}$ (20 periods).

Flow photographs were taken on Tri-X film with a Nikon 35mm camera mounted above the cylinder. A 22-watt flourescent circle lamp with parabolic reflector was fixed beneath the cylinder to provide back lighting. An adjustable sequence timer triggered the camera mechanism and dye production. The fractional variability of the switching pulses was estimated at $< 1 \times 10^{-3}$.

3.2 Flow Visualization Methods

Velocity measurements were made in the interior and western boundary layer over a wide range of Rossby and Ekman numbers, using sequence photography. The pH indicator Thymol Blue technique outlined by Baker (1966) was used in the linear flow regime where relative velocities were smaller than 0.1 cm/sec. Two identical grids (shown in Fig. 5) of fine .001" platinum-irridium wire were stretched horizontally across the cylinder at depths of 5.53 cm and 10.53 cm. The cylinder was filled with a 0.1 N solution of Thymol Blue titrated to its basic endpoint. Applying a small d.c. potential across the two grids changed the local pH around each wire, causing the fluid around the negative electrode to become more basic and turn a deep blue. A sequence of these dye lines was photographed as they were swept off the electrode (see Plate 1). Since the time interval for the dye to be formed and carried out of the boundary layer around the wire was not accurately known, the horizontal distance between successive dye segments was measured and divided by the sequence interval to compute the average observed velocity.

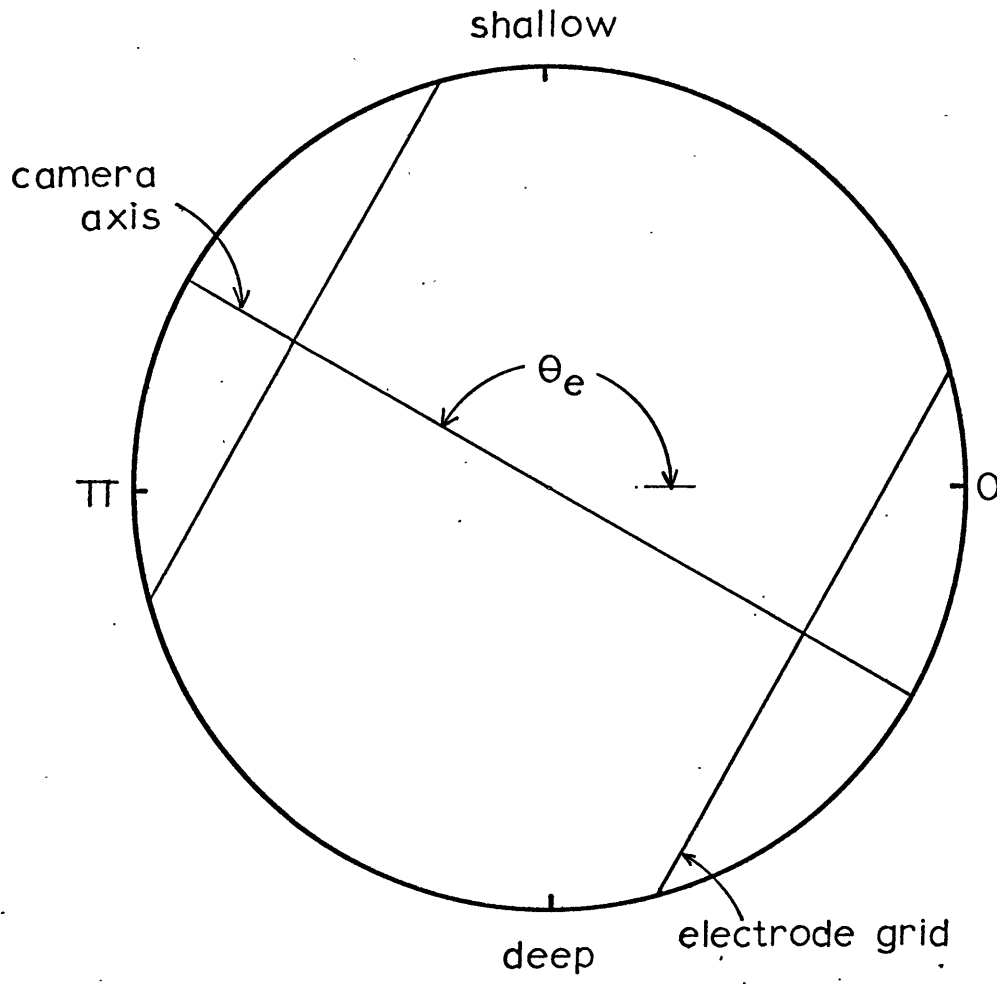The electrodes were aligned along the east-west axis for

FIGURE 5 . Horizontal cross-section of
electrode grid

the interior velocity measurements, so the distance between successive dye segments was measured perpendicular to the electrode to determine the geostrophic cross-contour flow component. Measurement of the western boundary layer velocity was complicated by two factors, curvature of the boundary and the dependence of the azimuthal velocity. The first was partially solved by digitizing the dye photograph and measuring the distance numerically along an arc of constant radius (see Appendix B). The second complication was circumvented by measuring the azimuthal velocity in the region $\theta = \pi$ where the least variation of v with θ occurred.

The non-linear flow regime was characterized by velocities of at least .01 cm/sec so two other flow visualization techniques were used. The horizontal structure was studied with streak photography using a water suspension of large aluminum flakes illuminated from the side by a light beam 1.39 cm thick. The beam was normally placed at a depth of 7.90 cm but was also placed at 3.28 cm (slit width = 1 cm) and 9.24 cm (slit width = 1 cm) to test the two-dimensionality of the flow.

The stability study was conducted using a sequential dye method. The cylinder was filled with a saturated starch-iodine solution and a fine stainless steel electrode (.025 cm outside diameter, 5.5 cm long) placed in the western boundary layer at $\theta = \pi$. A periodic potential was applied to the electrode, causing a long sequence of dye pulses to be formed in the western boundary layer. The pulses were carried through the western boundary layer to the transition region where they were photographed periodically. The stable mode was characterized by excellent repeatability while the unstable mode exhibited a periodic temporal variation of the dye pattern.

Separate experiments conducted to check the electrode's influence on the onset of instability indicated that the stability results were unchanged by either (a) a shift in the azimuthal position of the electrode in the western boundary layer to $\theta = 7\pi/6$ at two different rotation rates or (b) substitution of a second, 20% thicker electrode at $\theta = \pi$. Also, the local

Reynold's number based on the diameter of the electrode never exceeded 8 at the critical Rossby number, so any distortion due to the electrode size and position was considered negligible.

The number of fluid solutions used and the variability of room temperature necessitated an accurate determination of the kinematic viscosity for each experimental run. The viscosity of each stock solution was measured over a $20^o - 25^o C$ temperature interval using a calibrated Fiske-Canon viscosimeter and a calibrated copper-constantin thermocouple. A second matched thermocouple was attached to the fluid container in the eastern boundary layer. The induced emf was measured though sliprings during each experiment, indicating that the fluid temperature remained constant to ± 0.03 °C over the duration of each experimental run.

The experimental procedure for these studies was similar. After transmission warm up, the table speed was set and a spin up period of $8\pi/2E^{1/2}\Omega$ (about 16 minutes for $\Omega = 3$ rad/sec) was allowed for the stability study and $4\pi/2E^{1/2}\Omega$ for the other studies. Then the glass disk was set in motion and after a similar spin up period, the flow observations were made and experimental parameters measured.

3.3 Experimental Error

The principal uncertainties in the velocity measurements arose in the data reduction process. The precise location of the leading edge of the dye line was difficult to locate on some of the enlarged photographs. Small random variations in the turntable's angular velocity also caused noticeable velocity deviations among the photographs, so a sequence of 8 photographs was interpreted and the mean and standard deviation values presented. Except for an estimated 1.8 to 2.9% uncertainty in $\tan\alpha$, the experimental parameters attributed less than a 1% uncertainty to the velocity calculations.

Measurements of the western boundary layer vortex positions and topographic half wavelengths on the enlarged streak photographs were complicated by the lack of a reference length and the difficulty of locating the cylinder axis in the photograph. A

sequence of 4 photographs was read to reduce the random errors involved, and the mean and estimated standard deviations presented.

The distinction between stable and unstable flow was occasionally clouded by the presence of aperiodic motion attributed to small variations in the turntable's angular velocity Ω. These runs were repeated under similar experimental conditions and the flow state then decided. A major experimental uncertainty arose in determining the formation period T of the unstable mode from the sequence photographs. A visual interpolation had to be made between photographs since T was rarely a harmonic of the sequence interval between successive photographs. This, coupled with the limited number of cycles photographed, caused typically an experimental uncertainty of $\sim$ 8% in the period measurements.

4. Experimental Results and Discussion

The first set of experiments to be described was designed to test the linear theoretical predictions presented in Section 2. Measurements were made of the cross-contour flow component in the interior and the azimuthal velocity profile in the western boundary layer. The second set of experiments described here was intended to indicate how the flow is modified by an increased driving stress. This set included a visual study of the horizontal velocity structure and determination of the critical parameter values for the onset of instability.

4.1 Interior Flow

The cross-contour velocity V_{CC} was measured at an interior point ($r' = 0.566$, $\theta_e = 0$, $z = .826$) as a function of α and ϵ. A second measurement was made at the lower point ($r' = 0.566$, $\theta_e = 0$, $z = .434$) to check the predicted z-dependence. The results presented in Fig. 6 and Table 1 indicate that the theoretical Sverdrup balance (18) accurately determines the two-dimensional cross-contour velocity component over the wide range of ϵ studied. While experimental uncertainties excluded actual measurement of the secondary interior flow parallel to the depth contours, the predicted sign and order of magnitude of this flow was observed to be correct.
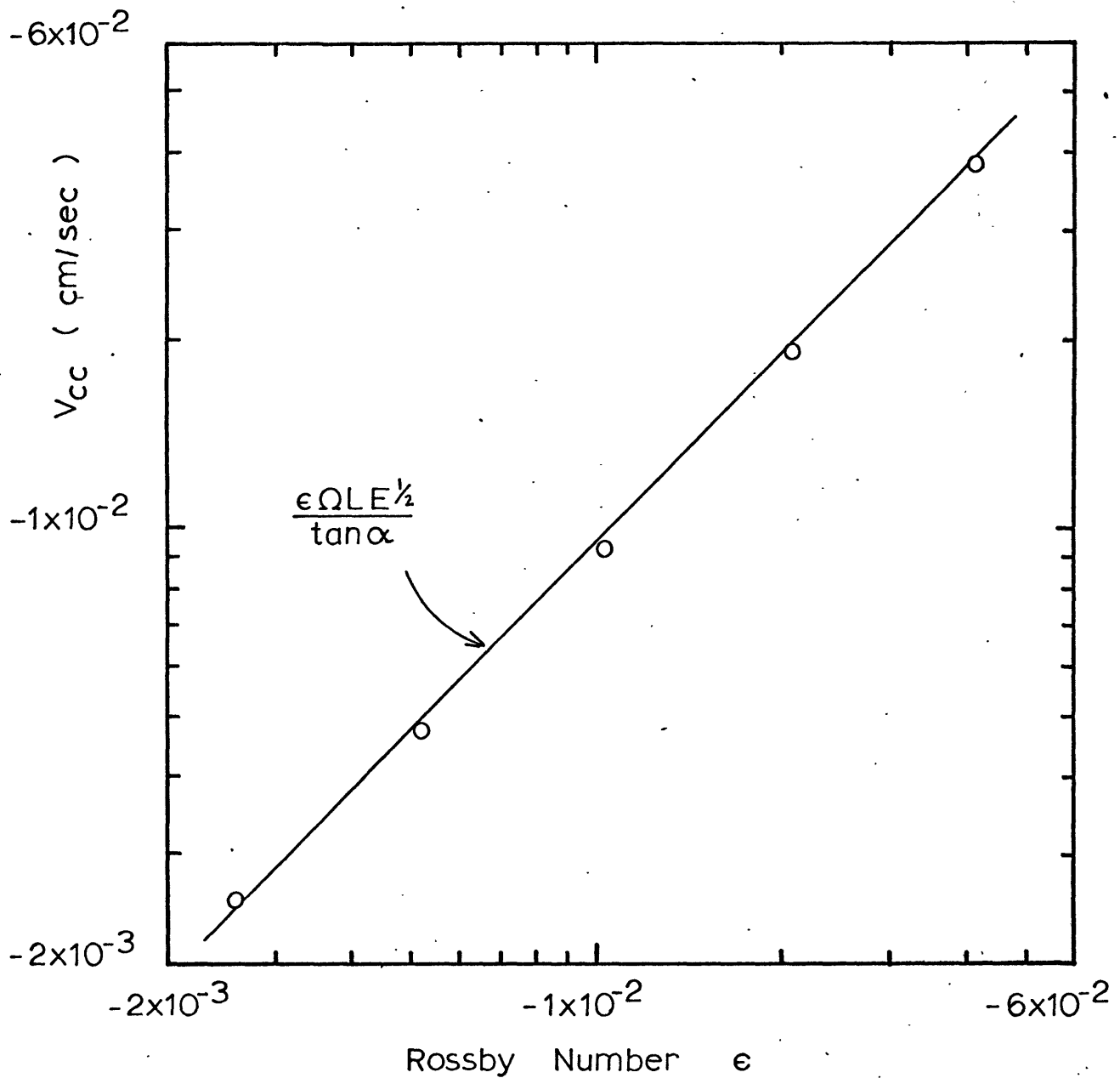
FIGURE 6. Interior cross contour velocity V_{cc} as a function of Rossby number ϵ. Theoretical value —, experimental points o, for $\tan\alpha = 178$, $\Omega = 3.03$ rad/sec., $E = 1.87 \times 10^{-5}$, ($\Theta_e = 0$, $r = 0.566$, $z = 0.826$).

ϵ

ϵ	tan α = 0.178	0.144	0.111
-.0416	z_1: 39.0±.8 (38.0±1.)		
-.0208	z_1: 19.6±.4 (19.3±.6)		
-.0104	z_1: 9.8±.2 (9.3±.3)		
-.0052	z_1: 4.9±.1 (4.7±.2)		
-.0026	z_1: 2.45±.05 (2.53±.08) z_2: 2.43±.05 (2.58±.12)	z_1: 3.02±.06 (3.20±.2)	z_1: 3.89±.08 (3.8±.1)

Experimental Conditions

Ω = 3.03 rad/sec

E = 1.87 x 10^{-5}

L = 12.75±.04 cm

θ_e = 0

Z_1 = 0.566

Z_2 = 0.826

Z_3 = 0.434

( ) indicates theoretical value computed from (18)

velocity unit = 1 x 10^{-3} cm/sec

TABLE 1 . Comparison of Interior Cross-Contour Velocity V_{CC} with Theory for Different Bottom Slope, Rossby Number, and Vertical Position.

4.2 Western Boundary Layer Flow

The azimuthal velocity profile V(r) was measured in the eastern boundary layer region near ($\theta_e = \pi$, z = .826) with the $\sim 10°$ sloping bottom for twelve different values of the main rotation rate Ω . A typical dye photograph is shown in Plate 1 and the measured profile in Fig. 7. The radial position of the velocity maximum was then measured and a logarithmic plot made as a function of E, in Fig. 8. A least squares fit to the data gives the equation

$$\ln(10 \Delta r_{max}) = (1.50 \pm .02) + (.34 \pm .02) \ln 10^5 E$$

which is in good agreement with the theoretical value

$$\ln(10 \Delta r_{max}) = (1.54 \pm .01) + (.33) \ln 10^5 E$$

found from (23) for $\theta = \pi$. A similar least squares analysis for the amplitude of the velocity maximum indicates that

$$\ln(10 V_{max}/E\Omega r_0) = (1.79 \pm 0.02) + (.21 \pm .02) \ln 10^5 E$$

in comparison to the predicted dependence

$$\ln(10 V_{max}/E\Omega r_0) = (1.86 \pm .01) + (0.166) \ln 10^5 E$$

based on (23). The discrepancy is probably attributable to the neglect of the higher order perturbation terms in the theoretical analysis.

The tangential velocity was also measured at four other azimuthal positions in the western boundary layer to check the predicted θ-dependence. Fig. 9 shows a comparison between the observed velocity maximum and the theoretical maximum calculated from (23). While the observed points correlate well with the theoretical envelope, the observed values nearer $\theta = \pi$ were from ~ 6 to $\sim 14\%$ smaller than predicted. The horizontal width of the experimental uncertainty bracket in Fig. 9 indicates the angular separation of the two sucesssive dye lines during the experiments.

The azimuthal velocity was also measured at the lower position ($\theta_e = \pi$, z = 0.434) to test the predicted two-dimensionality of the western boundary layer. The profiles shown in Fig. 10

PLATE 1 : Azimuthal velocity in western boundary
layer for ~10° sloping bottom. Experimental
conditions correspond to figure 7; ($\theta_e = \pi$,
z = 0.826). Interval between dye pulses is
25 seconds. Radial distance along electrode
between side wall and cross wire provides
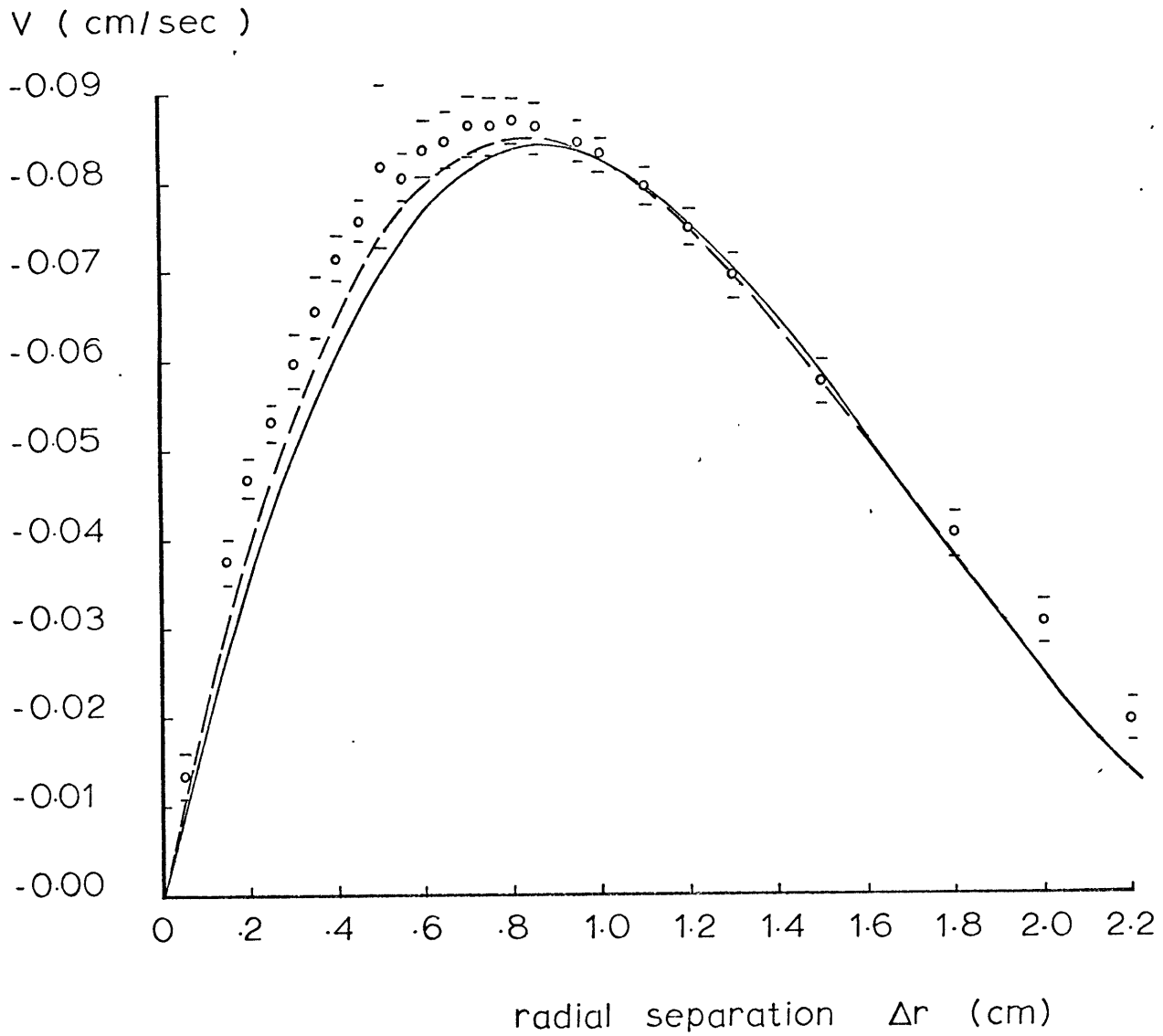reference length in photograph.

FIGURE 7. Western boundary layer velocity profile. Theoretical profile (first order)--, (second order)——, experimental points ∘, for $\tan \alpha = \cdot 178, \Omega = 1 \cdot 03$ rad/sec., $\epsilon = -\cdot 0076$, $E = 5 \cdot 62 \times 10^{-5}, (\Theta_e = \pi, z = 0 \cdot 826)$.
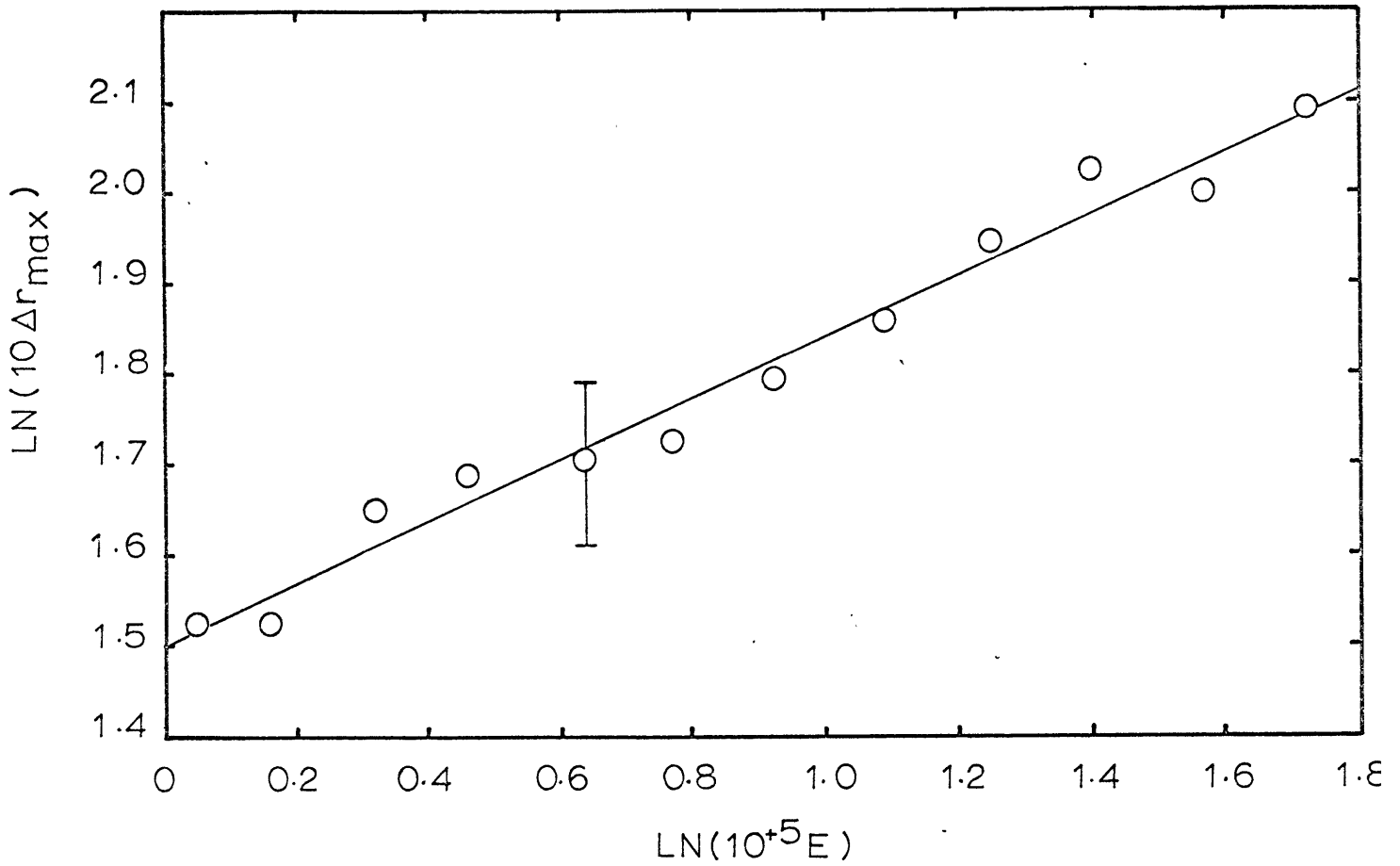
URE 8. Radial separation to western boundary layer azimuthal velocity maximum as a function of Ekman number E. Experimental points O, least squares linear fit ———, experimental uncertainity I, for $\tan\alpha = \cdot178$, $1\cdot03$ rad/sec $\leq \Omega \leq 5\cdot43$ rad/sec, $e\Omega = -0\cdot0078$ rad/sec, $(\Theta_e = \pi, z = 0\cdot826)$.
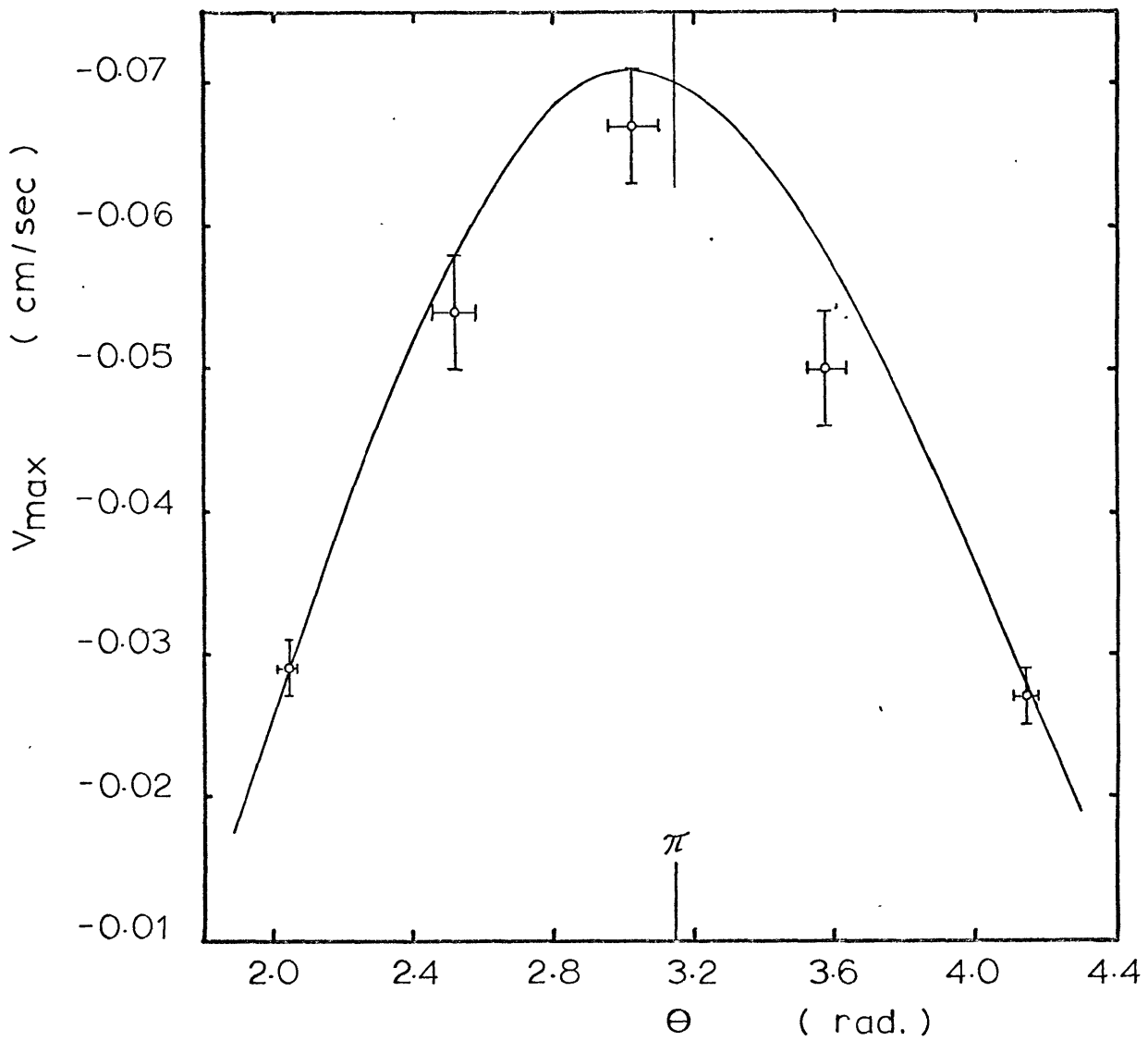
FIGURE 9. Western boundary layer azimuthal velocity maximum as a function of azimuthal position Θ. Theoretical envelope(second order)—, experimental points ○, uncertainity I, for $\tan\alpha = \cdot 178, \epsilon = -0.0026, \Omega = 3.03$ rad / sec., $E = 1.90 \times 10^{-5}, (\Theta_e = 2\pi/3, 5\pi/6, \pi, 7\pi/6, 4\pi/3, z = 0.826)$.
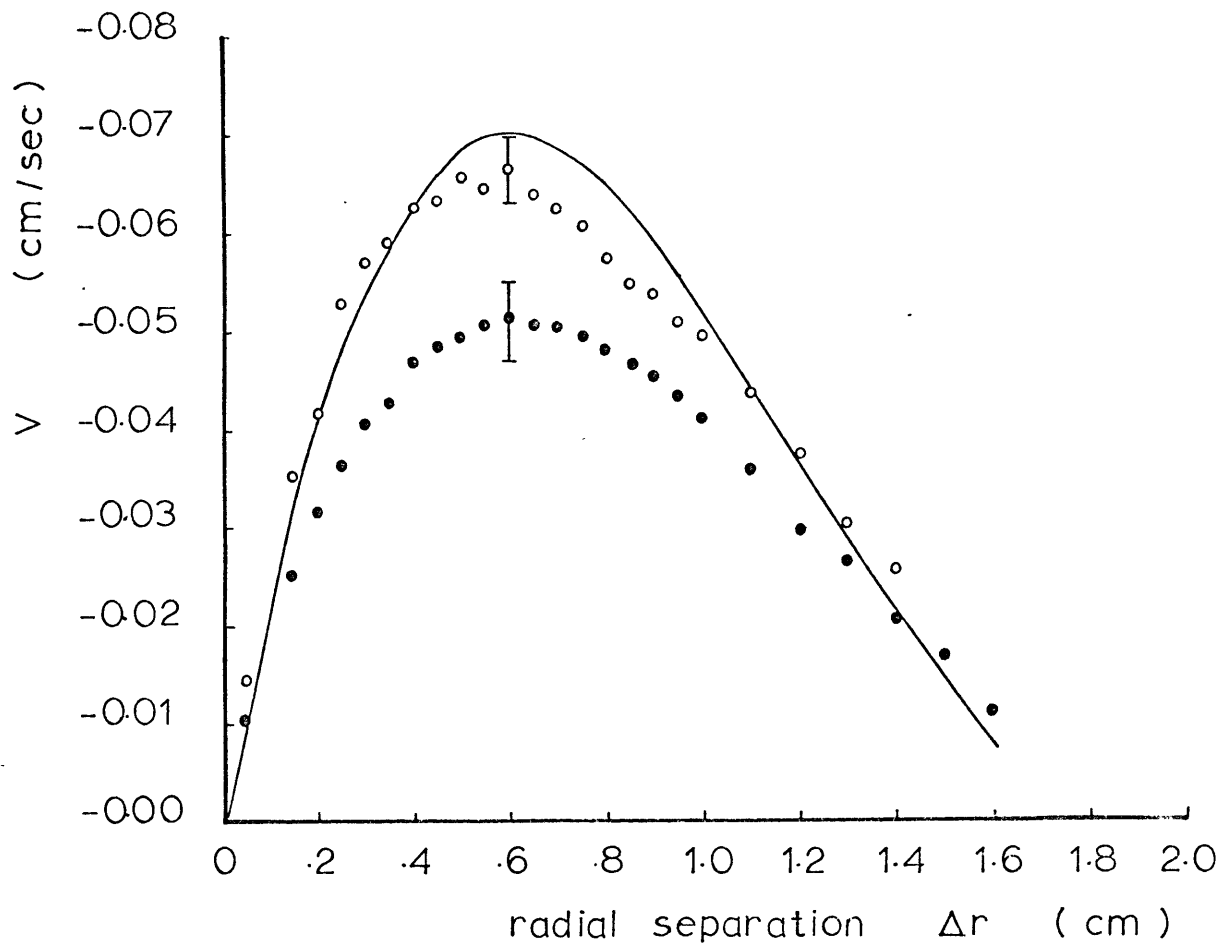
FIGURE 10 . Western boundary layer azimuthal velocity profile as a function of depth. Theoretical profile (second order) —, experimental points •(5·5 cm),∘(10·5 cm), uncertainity I, for tanα=-178, ε=-0·0026, Ω=3·03 rad/ sec, E=1·88×10^{-5},(Θ$_e$=π, z=0·434,0·826).

indicate a 27% variation in amplitude at the two vertical positions while the profiles are similar in form. The cause for this is unknown.

The azimuthal velocity profiles measured at ($\theta_e = \pi$, z = .826) for the two smaller bottom slopes are shown in Fig. 11. The sizable discrepancy between observed and (23) probably lies in the approximate and limited perturbation treatment of the linear theory.

4.3 Horizontal Structure in Non-Linear Regime

The non-linear flow regime in the sliced cylinder was marked by a more noticeable north-south asymmetry of the western boundary layer structure. As the driving stress was increased, a fluid particle in the western boundary layer acquired more inertia until it tended to overshoot its essentially interior equilibrium position. The particle then reversed its direction of flow and lost its excess inertia and vorticity through dissipation and stretching before returning to the interior.

This north-south distortion (illustrated in Plate 2) first became apparent for the $\sim 10^o$ sloping bottom when $|\epsilon|$ was increased past $E^{1/2}$. When $|\epsilon| \sim 3E^{1/2}$, part of the western boundary layer flow had closed upon itself to form a vortex in the northwest quadrant and when $|\epsilon| \sim 6E^{1/2}$, this vortex had shifted to $\sim 130^o$. A larger stress increased the boundary layer transport and the radial distance from the center of the vortex to the side wall but did not substantially affect the vortex's azimuthal position. Fig. 12 shows the movement of the vortex's center as was increased through different values. As the stress was increased, the azimuthal angle passed through a maximum value which was approximately the same for the three different bottom slopes. Additional measurements made at other depths are presented in Table 2 which indicate that the vertical axis of the vortex was aligned with the main rotation axis to within an estimated experimental uncertainty of $\pm 2.1^o$.

A fluid particle entering the interior from the western boundary layer went through a transition region where the inertia and extra vorticity acquired by non-linear processes in the western boundary layer were lost. The size of this region
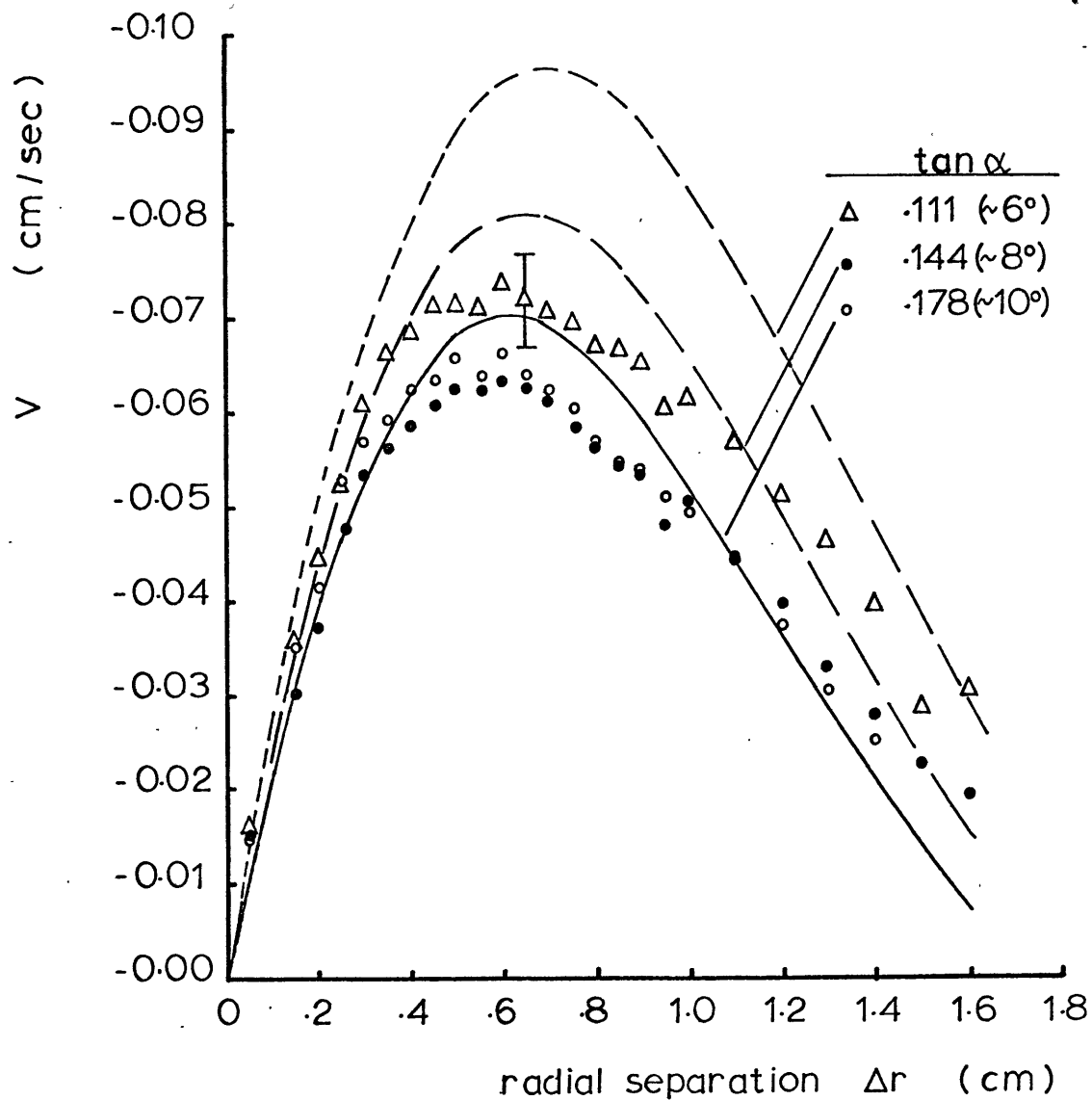
FIGURE 11 .Western boundary layer azimuthal velocity profile as a function of bottom slope. Theoretical profiles (second order), for $\varepsilon = -0.0026$, $\Omega = 3.03$, $E = 1.89 \times 10^{-5}$, $(\Theta_e = \pi, z = 0.826)$.
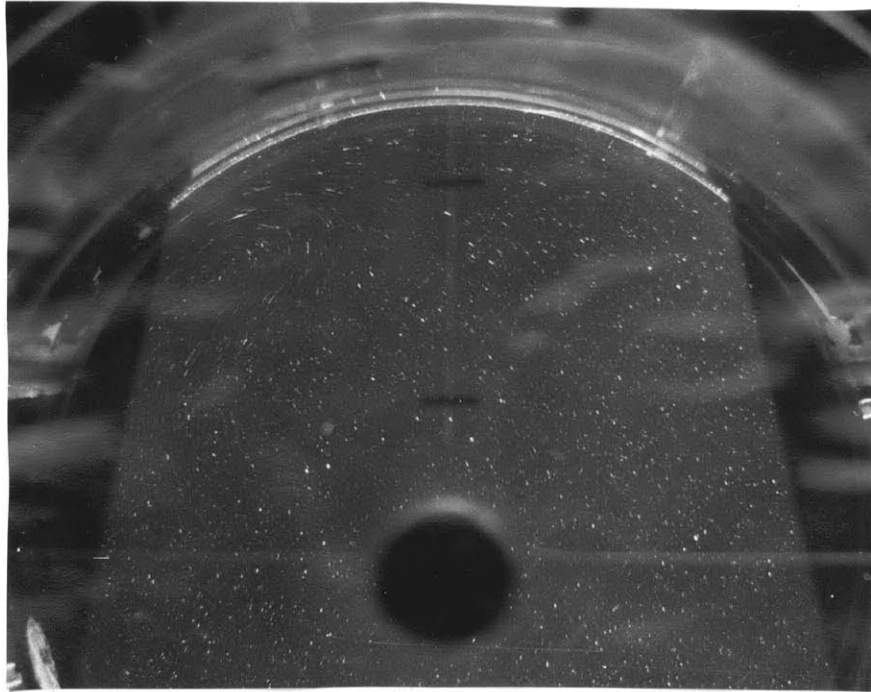
(a) $\epsilon = -.0190; |\epsilon|/E^{\frac{1}{2}} = 4.21$

PLATE 2: Horizontal velocity structure in
northern half of basin for 10 sloping
bottom. Experimental conditions: tan α =
.178, Ω = 3.03 rad/sec, E = 2.03 x 10^{-5},
(z = 0.62), exposure time was (a) 4.88
sec, (b) 3.25 sec, (c) 3.25 sec.
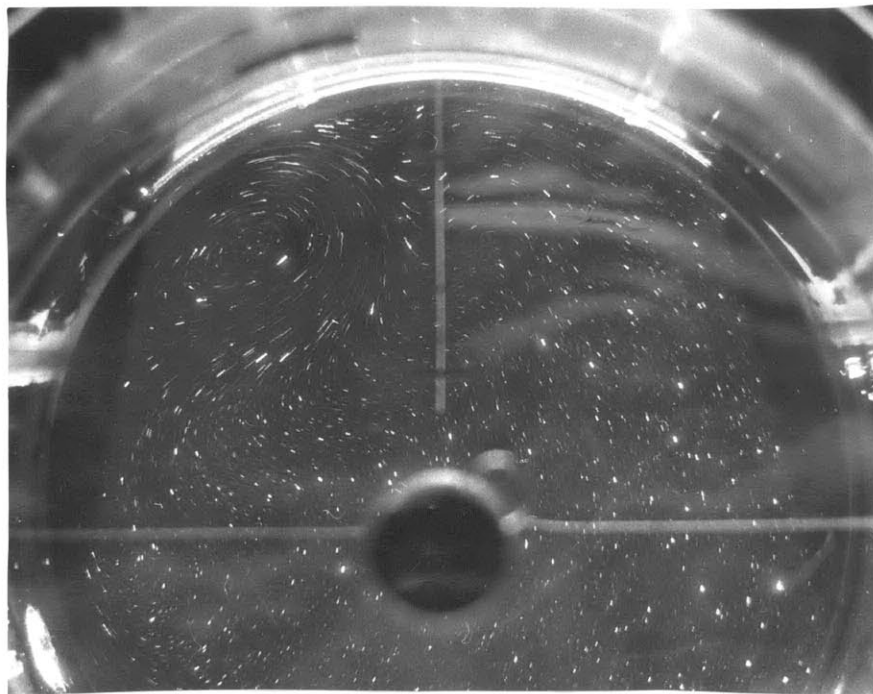
(b) $\epsilon = -0380; |\epsilon|/E^{1/2} = 8.43$
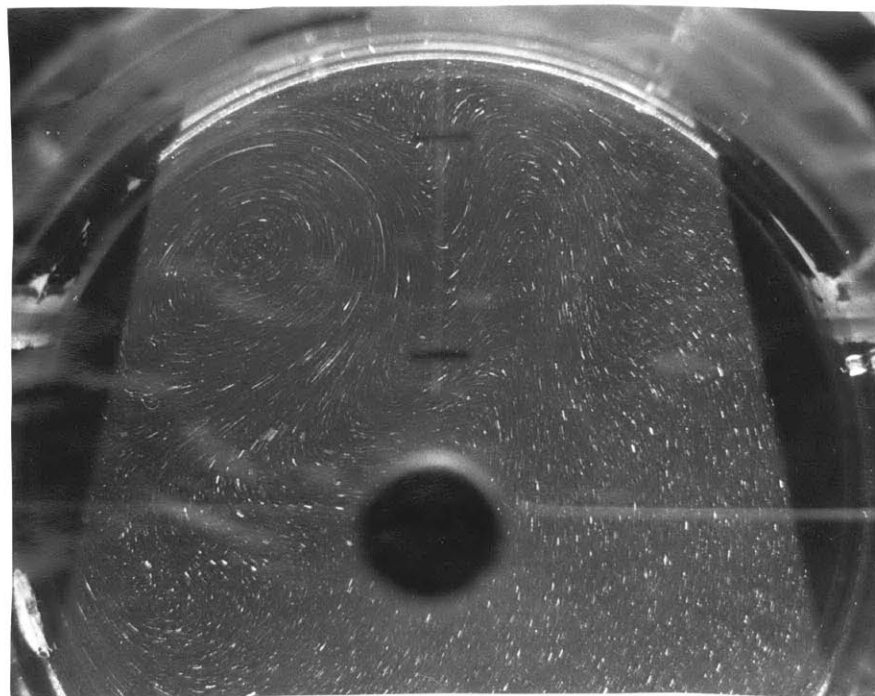
(c) $\epsilon = -.0596; |\epsilon|/E^{1/2} = 13.21$

PLATE 2 (continued)
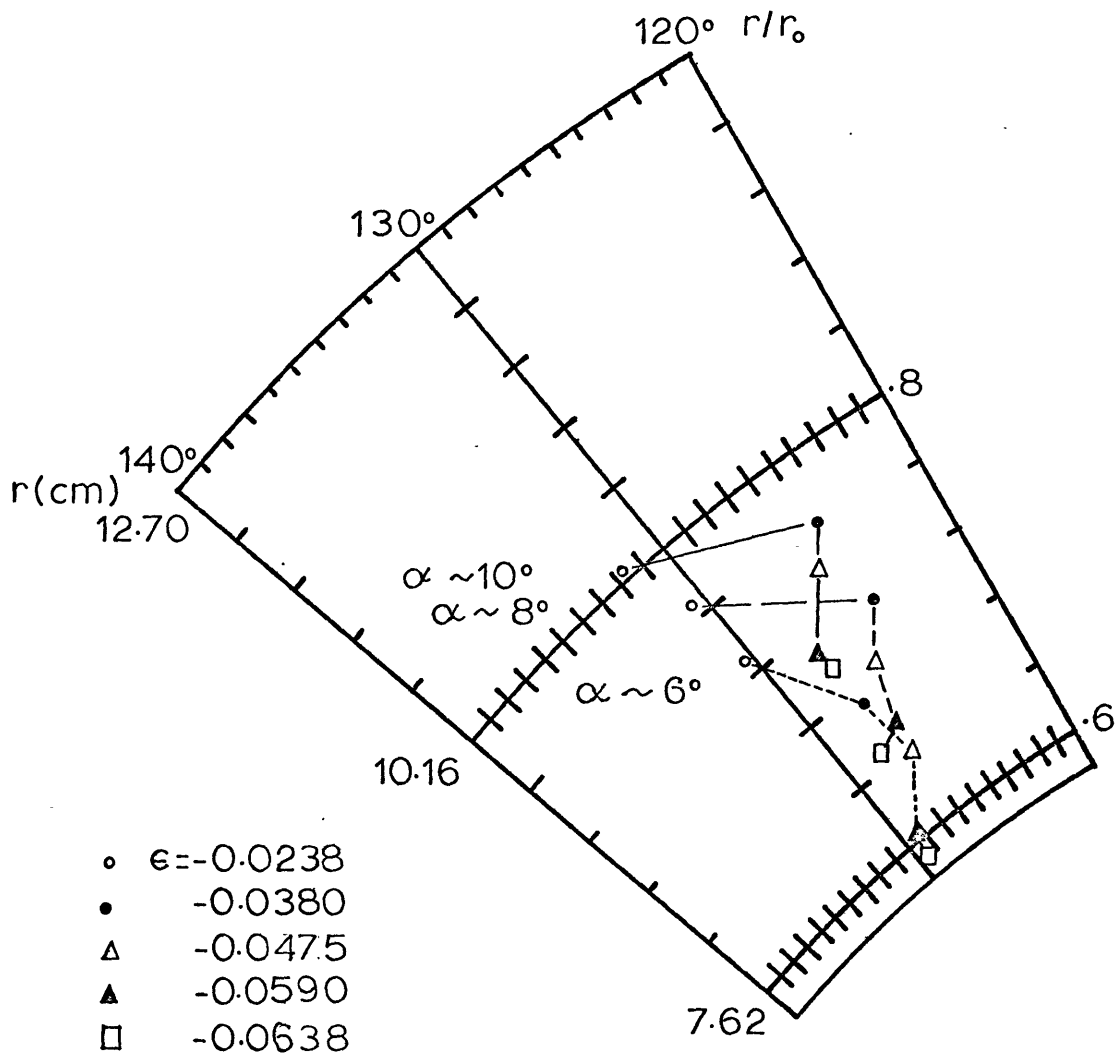
FIGURE 12. Western boundary layer vortex position as a function of Rossby number and bottom slope. $\Omega = 3.03$ rad/sec., $\bar{E} = 2.04 \times 10^{-5}$, ($z = 0.62$).

	.111	.144	.178
−.0637	z_2:(7.5±.1,129.4°±.3°)	z_2:(8.23±.05,128.1°±.4°)	z_2:(8.82±.08,127.8°±.3°)
−.0596	z_2:(7.6±.1,129.1°±.2°)	z_2:(8.31±.06, 127.0±.4°)	z_1:(8.99±.05,129.0°±.9°) z_2:(8.97±.08,128.0°±.4°) z_3:(8.97±.05,129.0°±.1°)
−.0475	z_2:(8.1±.1,127.2°±.4°)	z_2:(8.69±.09,126.0°±.3°)	z_1:(9.4±.1 ,126.1°±.7°) z_2:(9.42±.08,125.9°±.5°) z_3:(9.32±.08,126.0°±1.°)
−.0381	z_2:(8.5±.1,127.7°±.5°)	z_2:(9.07±.06,124.8°±.2°)	z_2:(9.7±.1,124.9°±.5°)
−.0238	z_2:(9.2±.1,130.4°±.7°)	z_2:(9.70±.06,130.5°±.4°)	z_2:(10.2±.1,131.7°±.9°)

$\tan\alpha$

Experimental Conditions:

Ω = 3.03 rad/sec z_1: .725 (slit width = .079)
E = 2.04 x 10^{-5} z_2: .620 (slit width = .109)
L = 12.75 ±.04 cm z_3: .256 (slit width = .079)

(r,θ) = (radial position (cm), azimuthal angle (degrees))

TABLE 2 . Position of Vortex in Western Boundary Layer for Different Values of Bottom Slope, Rossby Number, and Vertical Position.

grew as the stress grew until topographic Rossby waves appeared (see Plate 2 b,c).

The topographic wave mechanism may be understood by consider- ing the tendency of a fluid column to preserve its absolute angular momentum (potential vorticity) as it leaves the western boundary layer. When ε is negative (to correspond to the experiments), a fluid column leaves the viscously dominated inner region of the western boundary layer next to the side wall with positive relative vorticity. As the column is advected southward through the transition region, the motion across the depth contours causes a stretching of the fluid column and a positive increase in its vorticity. If the vorticity gain is larger than loss by lateral diffusion and Ekman layer suction, the column acquires cyclonic curvature and the streamline curves back toward the shallow end. The column is now compressed and gains negative relative vorticity until its path becomes anticyclonic and curves again toward the deep end. Net vorticity loss keeps the column from returning to its original depth contour.

The gross structure of these topographic waves can be obtained from a simple two-dimensional model where the rate of relative vorticity change is balanced by the stretching or shrinking of the fluid column. The potential vorticity equation yields for an east-west plane wave solution the familiar dispersion relationship

$$\sigma = - \frac{2\Omega}{L} \tan\alpha \frac{1}{k}$$

The wave fronts travel westward with a phase speed $C_p = -\frac{2\Omega}{Lk^2}\tan\alpha$ while the energy propagates eastward with a group speed $C_g = -C_p$. Superimposing these dispersive waves on a uniform eastward current U (along the depth contours) results in a stationary streamline pattern provided the relative wave speed vanishes, i.e., $U + C_p = 0$. This selects a single wave number which chooses the wave length of the stationary topographic wave

$$\lambda_s = 2\pi \sqrt{\frac{UL}{2\Omega \tan\alpha}}$$

While the observed flow was far more complex, the model appeared to approximate the flow best in the transition region near the boundary layer vortex where variation in the y-direction

appeared to be a minimum. The distance along the depth contour through the boundary layer vortex between the two successive points where $\vec{u} \cdot \hat{\jmath} = 0$ was identified as the observed half wavelength. With V estimated to be $\epsilon \Omega L E^{1/2}/\tan\alpha$, the predicted half wavelength becomes

$$\frac{\lambda}{2} = \frac{\pi L}{\sqrt{2}} \frac{E^{1/4} \sqrt{\epsilon}}{\tan\alpha} \tag{24}$$

The half-wavelength was measured at several depths for the three sloping bottoms; the results are compared with (24) in Table 3 and in Fig. 13. While the model is clearly inadequate, the $\sqrt{\epsilon}$ dependency was observed as was a general increase in half wavelength with decrease in bottom slope.

4.4 Onset of Instability

As the applied stress was increased, a critical value of ϵ was reached for which the steady flow was unstable. The velocity field was characterized by a small oscillation of the western boundary layer vortex and the periodic formation and decay of a second vortex or eddy in the transition region. A sequence of 4 photographs in Plate 3 shows this formation and the subsequent movement and decay of the second eddy over approximately one period for the $\sim 10^\circ$ sloping bottom. Measurements made at two depths ($z = .725$, $.256$) indicated that the curve swept out by the center of this second vortex was independent of z. Both the western boundary layer vortex and the second vortex were two-dimensional.

Bryan(1963) showed in his β-plane analysis of the wind-driven ocean circulation that Reynolds numbers based on the western boundary layer current and interior flow are equivalent since the western boundary layer and interior horizontal transports are equal by continuity. The equivalent interior Reynolds number for the sliced cylinder model is

$$Re = \left| \frac{V_\alpha L}{\nu} \right| = \frac{|\epsilon|}{\tan\alpha \, E^{1/2}}$$

Two sets of stability tests were made to determine the dependence of Re_c, the critical value at initial onset of instability, on the bottom slope and Ekman number. In the first set the Rossby

ϵ

	$\tan\alpha = .111$	$\tan\alpha = .144$	$\tan\alpha = .178$
$-.0637$	$z_2:3.07\pm.05$ (4.32)	$z_2:2.79\pm.03$ (3.34)	$z_2:2.41\pm.1$ (2.71)
$-.0596$	$z_2:2.92\pm.03$ (4.18)	$z_2:2.77\pm.05$ (3.23)	$z_1:2.31\pm.05$ (2.61) $z_2:2.36\pm.08$ (2.61) $z_3:2.34\pm.05$ (2.61)
$-.0475$	$z_2:2.7\pm.1$ (3.73)	$z_2:2.49\pm.05$ (2.88)	$z_1:2.11\pm.05$ (2.33) $z_2:2.21\pm.08$ (2.33) $z_3:2.14\pm.03$ (2.33)
$-.0381$	$z_2:2.36\pm.08$ (3.33)	$z_2:2.3\pm.1$ (2.81)	$z_2:1.93\pm.08$ (2.09)

$\tan\alpha$

Experimental Conditions

Ω = 3.03 rad/sec

E = 2 04 x 10^{-5}

L = 12.75 ± .04 cm

z_1 = .725 (slit width = .079)

z_2 = .620 (slit width = .109)

z_3 = .256 (slit width = .079)

( ) = theoretical value computed from (14)

TABLE 3 . Comparison of Observed Topographic Half
Wavelength, with Theory for Different Values
of Bottom Slope, Rossby Number, and Vertical
Position.

a) λ/2 versus ε
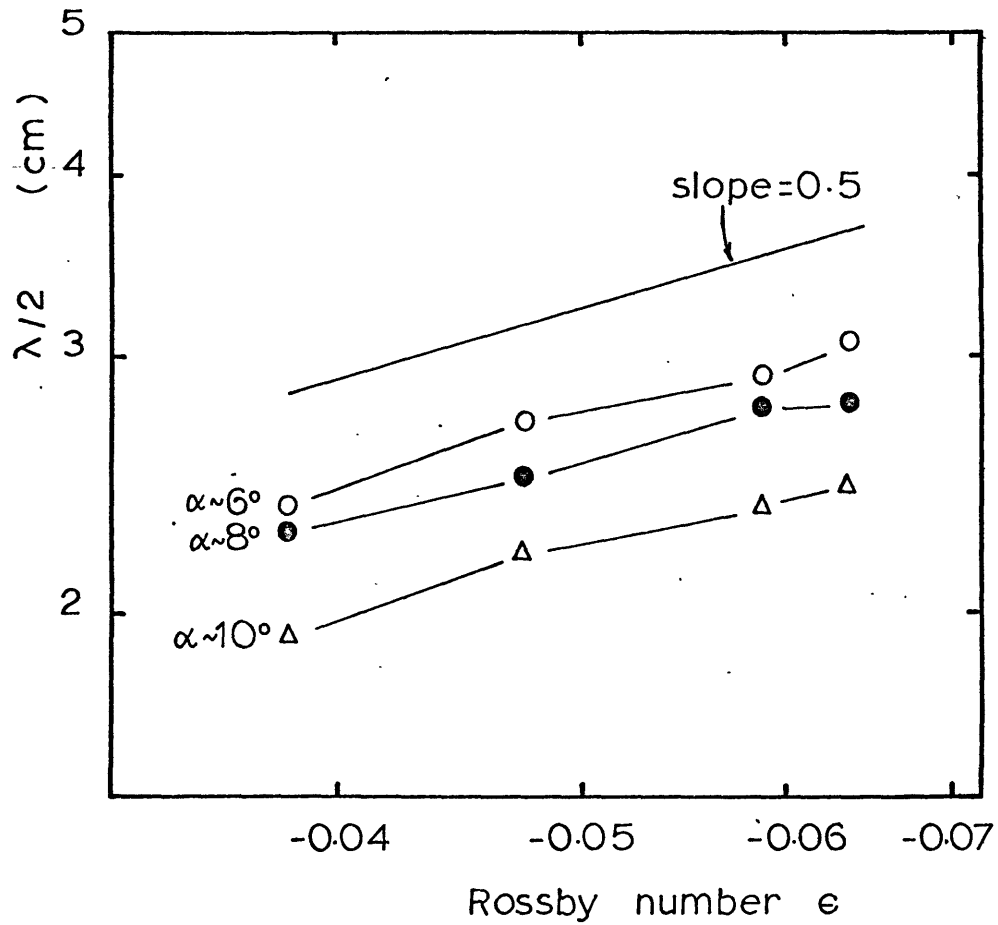
FIGURE 13. Topographic half wavelength as a function
of Rossby number and bottom slope.
$\Omega = 3.03\,rad/sec.$, $E = 2.05 \times 10^{-5}$, ($z = 0.62$).
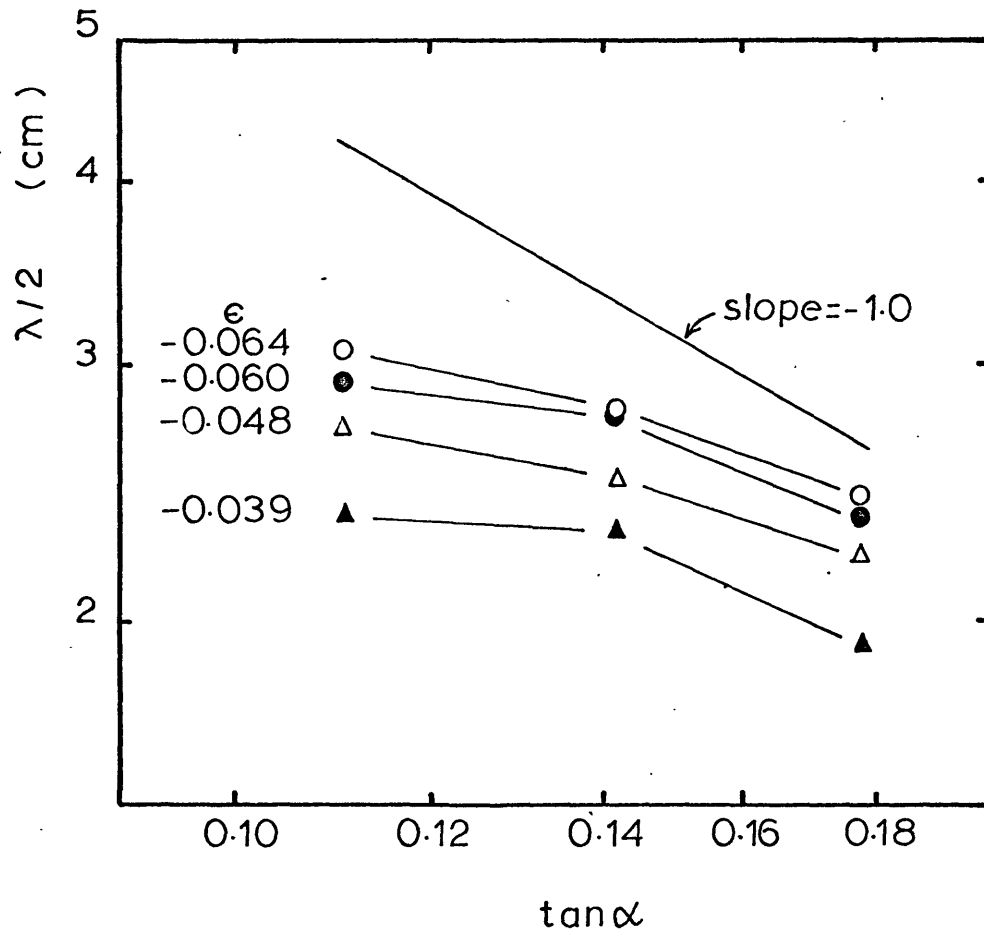
b) $\lambda/2$ versus $\tan \alpha$

FIGURE 13 (con't).

(a) t = 0
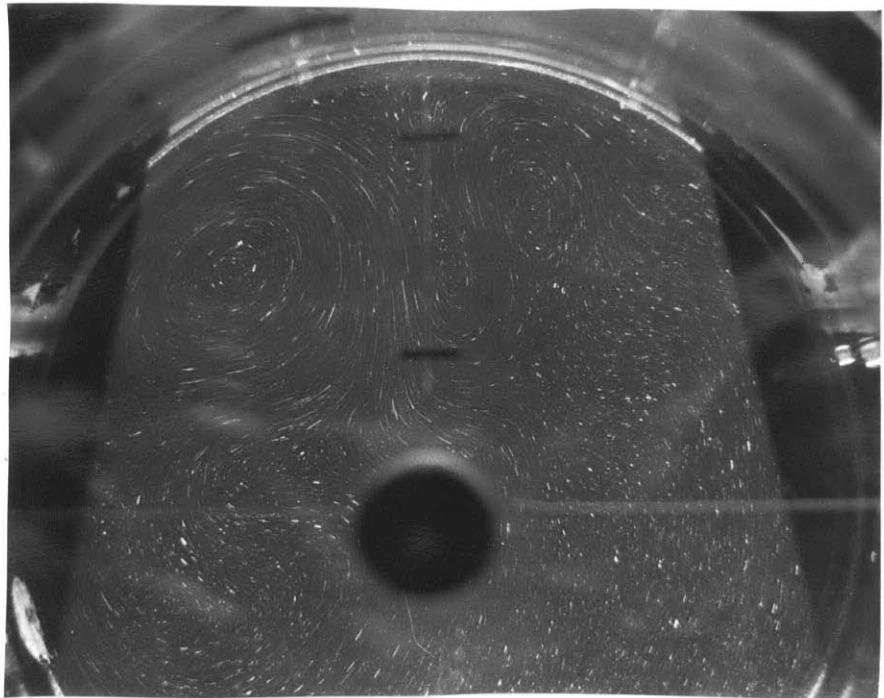
(b) t = 6.43 days
(13.33 sec)
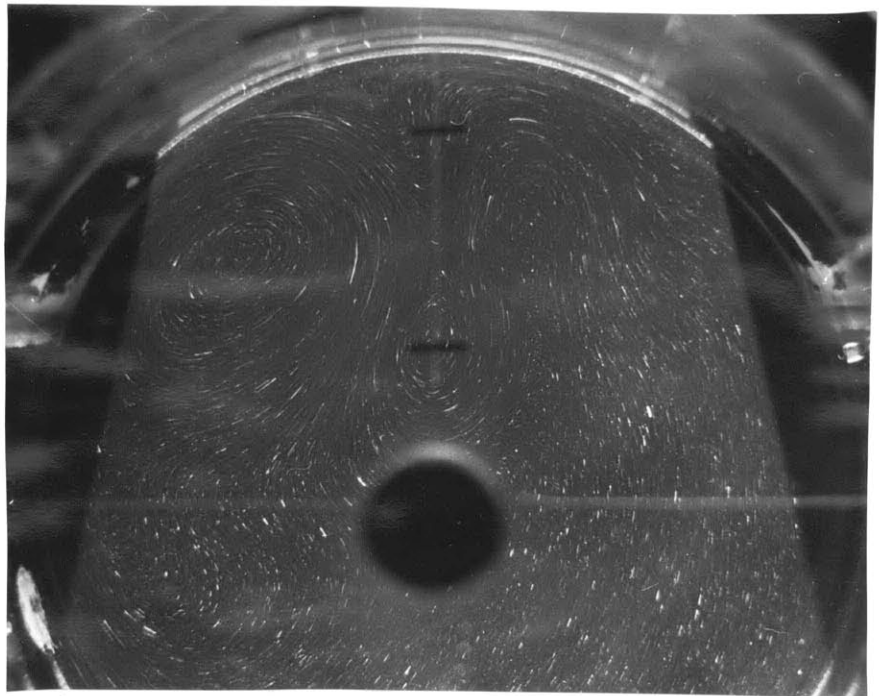
PLATE 3: Horizontal velocity structure for
unstable mode in northern half of basin
for $\sim10°$ sloping bottom. Experimental
conditions: tan α = .178, Ω = 3.03 rad/
sec, E = 2.04 x 10^{-5}, (z = 0.62), exposure
time = 3.25 sec. Approximate formation
period of second vortex is 23.5 days.
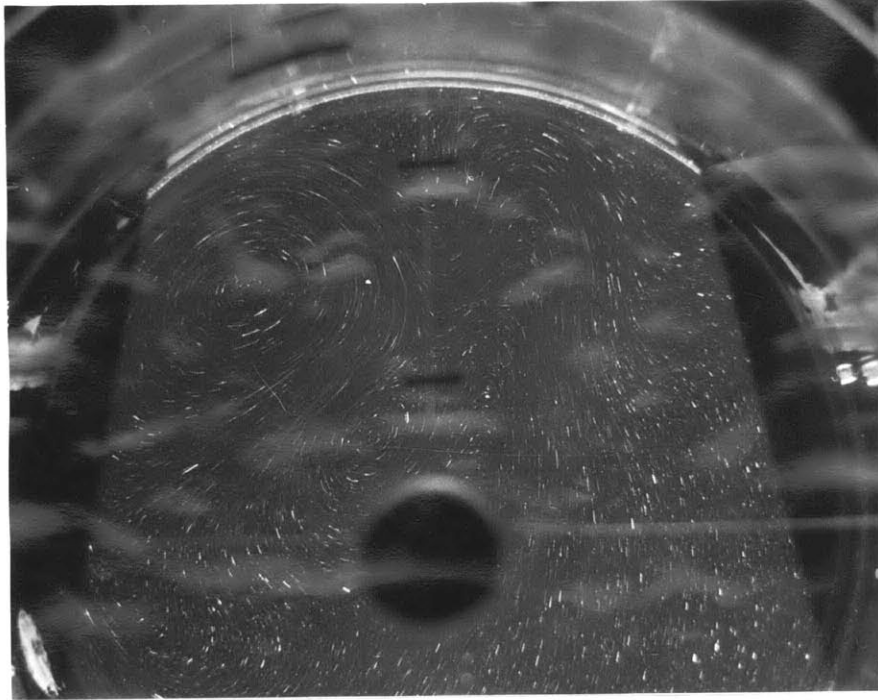
(c) t = 12.86 days (26.67 sec)
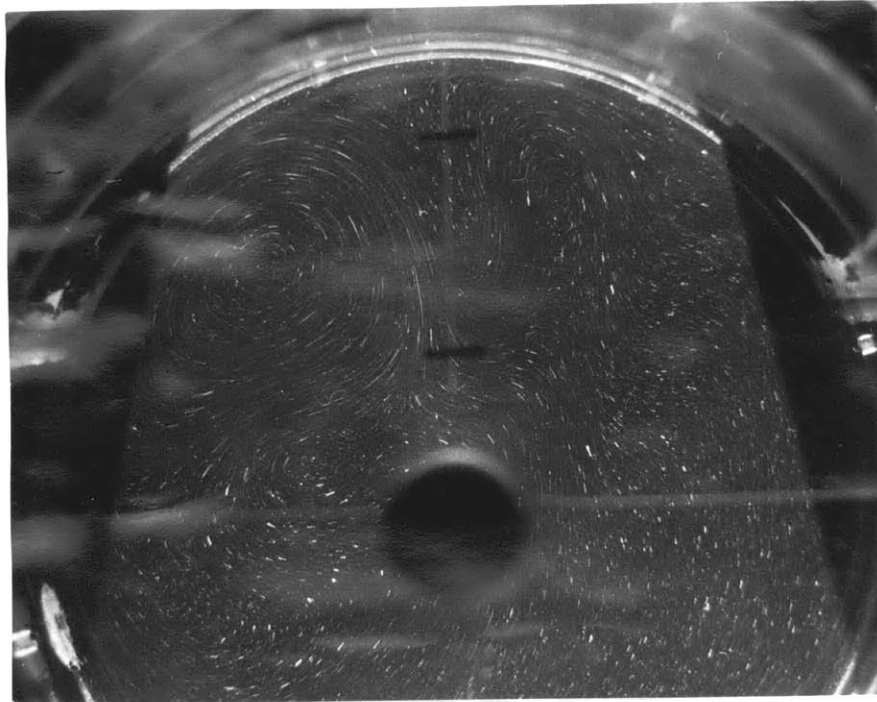
(d) t = 19.29 days (40.00 sec)

PLATE 3 (continued)

number and Ω were varied for the $\sim 10°$ sloping bottom. The results are shown in a stability diagram of Re versus E (Fig. 14) and indicate that

$$Re_c(\tan \alpha = .178) \simeq 63.5 + 7.17 \times 10^5 E$$

The dependence of Re_c on tan α was determined in the neighborhood of $E \sim 2 \times 10^{-5}$ in the second set of experiments. These results presented in Fig. 15 show that

$$Re_c (E = 2.14 \times 10^{-5}) \simeq \frac{14.05}{\tan \alpha}$$

The critical parameter determining the onset of instability over the ranges of ϵ, $\tan \alpha$, E studied then appears to be $|\epsilon|/E^{1/2}$ with the stability curve being

$$\tan \alpha \, Re_c = |\epsilon|/E^{1/2} \simeq 11.3 + 1.27 \times 10^5 E$$

Measurements of the unstable mode period T, i.e., the time interval between successive formations of a second vortex, indicate that T was also independent of tan α . The results shown in Fig. 16 fit the approximate equation

$$T \, (days) \simeq 32 \left(1 - \ln \left(10^5 E\right)^{\frac{1}{3}}\right)$$

Periods of the natural topographic Rossby modes for the sliced cylinder container found by Pedlosky and Greenspan (1967)

$$T \, (days) = \frac{L \, k_{mn}}{r_0 \, \tan \alpha} \quad \text{where} \quad J_m(k_{mn}) = 0$$

are similar in magnitude to the observed values but should be approximately independent of viscous effects and thus independent of E. This suggests that the instability mechanism may be associated with either the $E^{1/2}$ or $E^{1/3}$ layers and not with a breakdown in the steady topographic wave mechanism.

Several ideas lend further plausibility to this hypothesis. Since rotation constrains the flow outside the viscous boundary layers to be quasi-two-dimensional, a disturbance caused by a fluid instability in a viscous boundary layer will probably be carried into the interior as a two-dimensional disturbance regardless of the initial position of the instability, if it is a low frequency mechanism. Therefore, even though the horizontal velocity structure

FIGURE 14. Stability diagram; Reynolds number versus Ekman number. Linear stability curve—, experimental points •stable, ○ unstable, for tan α = ·178. (B) indicate Bryan's projected results.
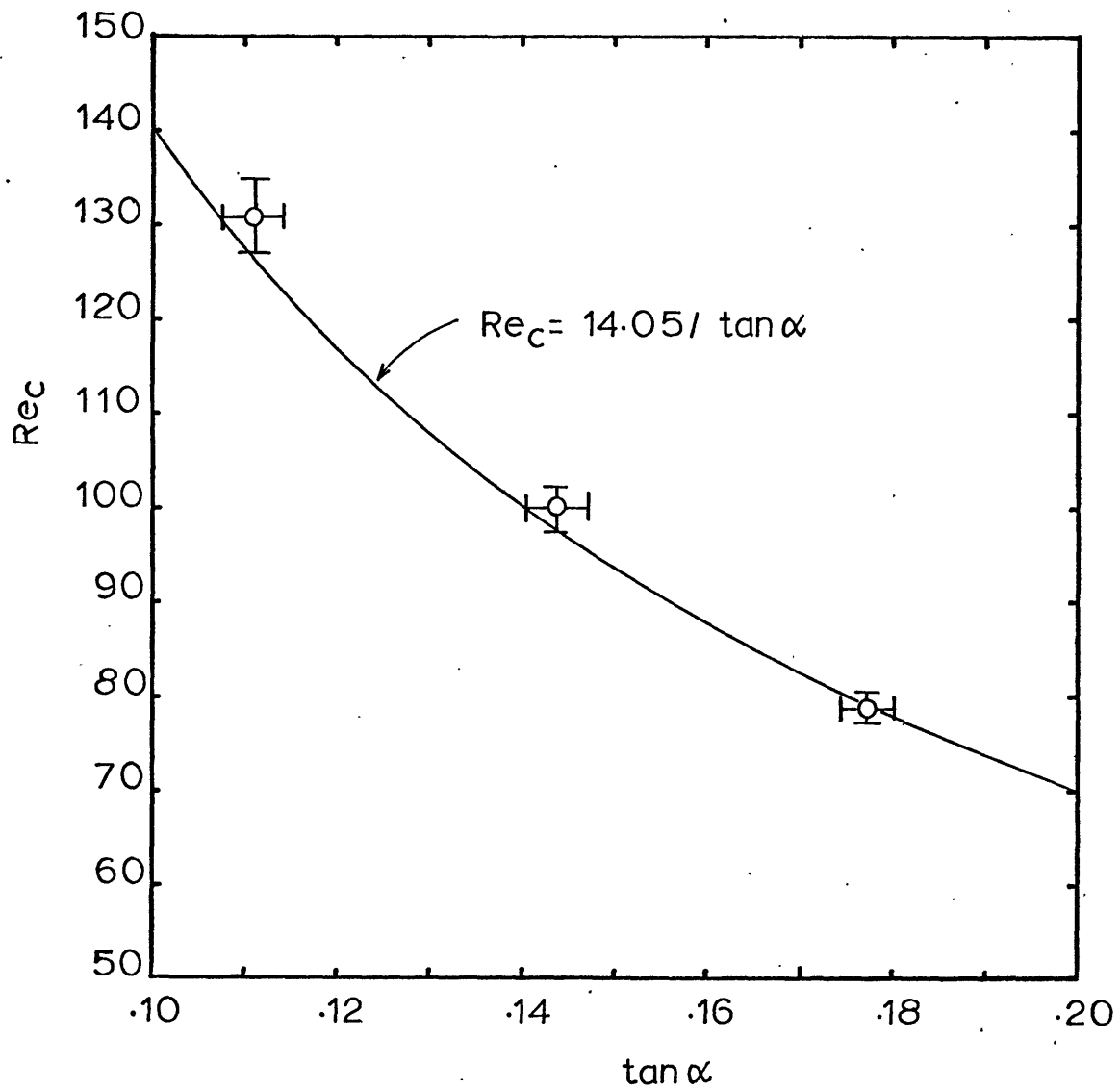
FIGURE 15 . Stability diagram; critical Reynolds number versus bottom slope. Experimental points o, uncertainity $\pm$, for $E = 2.14 \times 10^{-5}$.
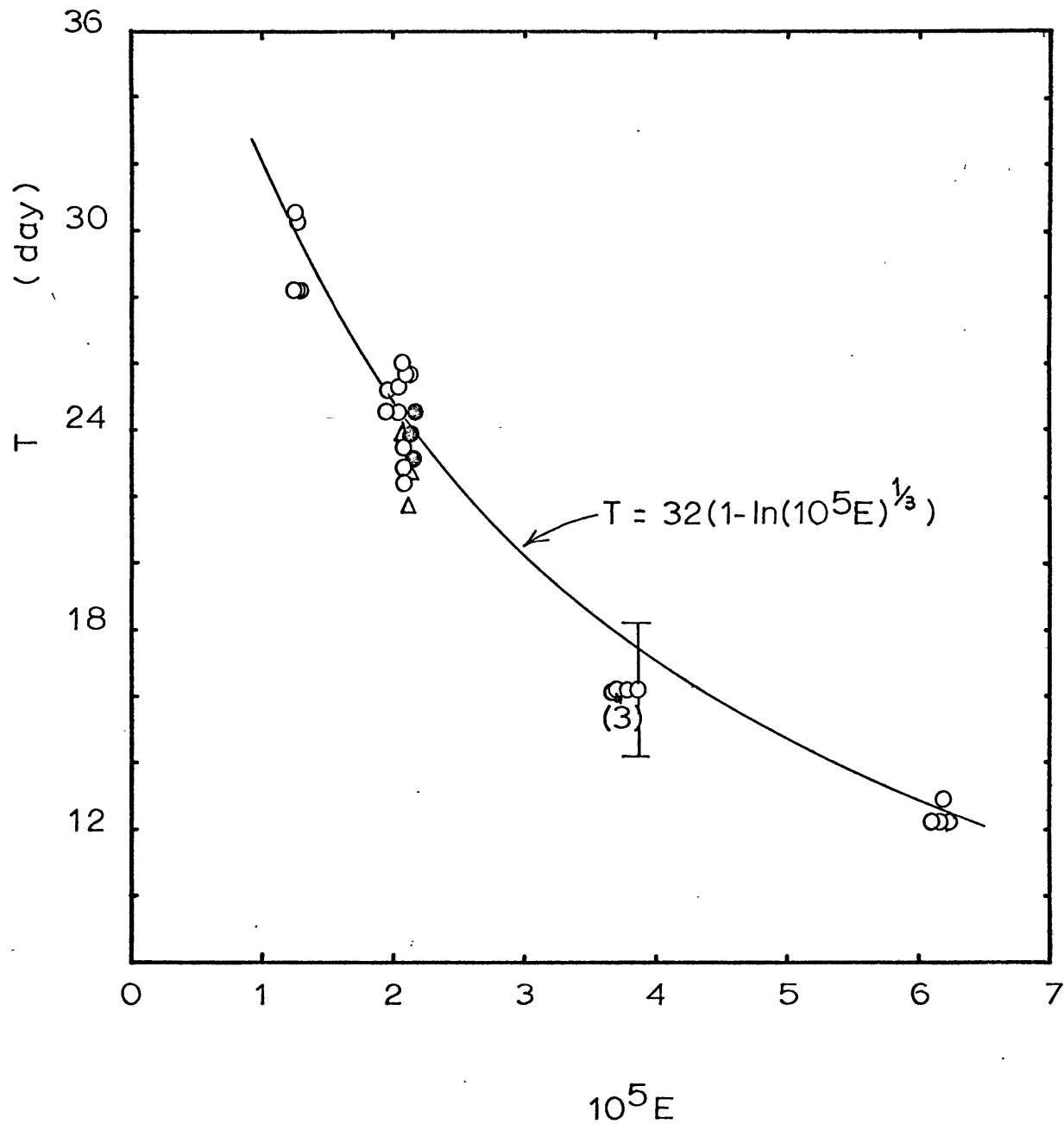
FIGURE 16. Observed unstable mode period. Experimental points o, typical uncertainity $\bar{\phi}$, for $\tan\alpha = \cdot178$, o for $\tan\alpha = \cdot144$, $\triangle$ for $\tan\alpha = \cdot111$.

in the unstable mode is observed to be independent of z in the boundary layer transition region and interior, the origin of the instability is still undetermined. Second, the observed instability appears to depend primarily on the parameter $|\epsilon|/E^{1/2}$ and not on $\tan\alpha$. The interior flow is clearly dependent on the bottom slope, but the flux into the top Ekman layer and down the normal $E^{1/3}$ layer is to lowest order independent of $\tan\alpha$. The Reynolds number based on this flux is

$$R_e^* = \left|\frac{\epsilon\Omega L \cdot L E^{1/2}}{\nu}\right| = \frac{|\epsilon|}{E^{1/2}}$$

i.e., the observed critical parameter. Since the Ekman layer instability discussed by Lilly(1966) occurs at values of Re > 50 and is of relative high frequency (typical periods are less than one day), and the velocity field is apparently only disturbed in the northern half of the basin, it seems that the observed instability originates in either the $E^{1/2} \times E^{1/2}$ corner region or the $E^{1/3}$ boundary layer along the western boudnary.

In conclusion, the experiments carried out suggest that the linear analysis presented in Section 2 is valid when ϵ is small enough ($\leq E^{1/2}$) that the inertial effects do not significantly affect the boundary layer vorticity balance. As ϵ is increased past $E^{1/2}$, the western boundary layer assumes an inner viscous, outer inertial boundary layer character, while the interior north-south flow continues to be given quite accurately by the Sverdrup balance. The western boundary layer first shows downstream intensification and then develops stationary topographic waves. Finally, as the critical value of Re^* or $\tan\alpha \cdot Re_{interior}$ is reached, a low frequency fluid instability is observed, probably attributable to a breakdown of the $E^{1/2} \times E^{1/2}$ corner region or the $E^{1/3}$ boundary layer structure.

5. Comparison with Previous β-Plane Models

Pedlosky and Greenspan (1967) have pointed out the striking similarity of the theoretical linearized flow in the sliced cylinder model to early β-plane solutions for the wind-driven ocean circulation problem. In particular are the linear solutions of Munk (1950) and Munk and Carrier (1950) who found

that the interior Sverdrup transport was closed by a strong
viscous western boundary current of width $\sim(\nu_e/\beta \cos\theta)^{1/3}$. Matching
their solutions to observed values of Gulf Stream transport and
width required such small values for the eddy viscousity para-
meter ν_e that the more recent studies have tended to concen-
trate on the non-linear dynamics that affect the western boundary
layer vorticity balance. The purely linear theories maintain
a balance in the western boundary layer between the negative
vorticity induced by the β-effect (or by vortex shrinking by
the bottom slope) and a horizontal viscous diffusion of positive
vorticity across the lateral boundary. In the purely inviscid
boundary layer theories, diffusion of vorticity is not present
so the fluid column itself must acquire negative vorticity as it
is carried northward in the western boundary current. This is
shown in the approximate vorticity balance $\mathcal{U}\,v_{xx} + \beta\,v \sim 0$
where existence of an inertial western boundary layer requires
the inertial term $\mathcal{U}\,v_{xx}$ to be negative to balance the positive
$\beta\,v$ term. Since the boundary current v increases toward the
lateral boundary, $v_{xx} > 0$ and $\mathcal{U} < 0$, indicating the interior
normal flux must be into the western boundary layer. This exis-
tence condition was illustrated in the inertial β-plane studies
of Fofonoff (1954), Morgan (1956), Charney (1955), and Carrier and
Robinson (1962) before a formal, more general derivation was given
by Greenspan (1962). This criterion applies to the sliced cylin-
der model, and indeed, accounts for the marked north-south
asymmetry of the western boundary layer in the non-linear flow
regime. As ϵ was increased and the inertial terms became more
important in the boundary layer vorticity balance, the interior
fed the boundary layer over a larger and larger arc until the
closed vortex formed in the northwest quadrant.

While the inertial boundary layer theories looked realis-
tic in the southern formation region of the western boundary
layer, they could not be used realistically in the northern
region to close the boundary layer flux to the interior. Ilyin
and Kamenkovich (1963) and Moore (1963) suggested that this circu-
lation may be closed in the northern half of the basin by imposing

damped, stationary Rossby waves on the eastward zonal outflux from the boundary layer. The more exact numerical studies by Bryan (1963) and Holland(1966) illustrate this mechanism.

In the sliced cylinder experiments, the horizontal circulation is closed by an analogous stationary topographic wave. The observation that the flow is steady suggests that these vorticity waves exert a stabilizing influence on the western boundary layer, for they allow a larger flux of vorticity to leave the boundary layer region via the wave mechanism than can be simply convected.

The observed sliced cylinder flow may be further compared with Bryan's (1963) numerical model of the western boundary current. He solved numerically the initial value problem for a homogeneous two-dimensional ocean in a rectangular basin with a Navier-Stokes dissipative term. At time zero, a steady wind stress is applied to an initially at rest ocean and the governing vertical vorticity equation integrated in time until a steady circulation pattern is reached. In the laboratory experiments, the driving stress was applied after initial spin up had occurred and the fluid had come to rest in the rotating coordinate system. Since the lowest order horizontal flows in both models obey the same approximate vertical vorticity equation (derived in Appendix E), Bryan's results may be compared for equivalent parameter values. The flow instability found by Bryan at $R\acute{e} = 100$ is qualitatively similar in description to the instability observed in the sliced cylinder experiments. A secondary vortex is periodically formed at a low frequency in the western boundary layer transition region where it is then swept downstream and decays. The general agreement shown in Fig. 14 may be fortuitous, though, since the probable source of the instability observed in the sliced cylinder model is the three-dimensional $E^{1/2} \times E^{1/2}$ corner or $E^{1/3}$ layer flow.

Acknowledgements

Bibliography

Baker, D.J. 1966. A technique for the precise measurement of small fluid velocities. J. Fluid Mech., 26, 573.

Beardsley, R.C. 1967. Design and construction of a stable laboratory turntable. Laboratory Note GFD/LN5, M.I.T., Cambridge, Mass.

Bisshop, F.E. 1966. Linearized flow in rotating systems. Technical Report No. 2, Brown Univ., Providence, R.I.

Bryan, K. 1963. A numerical investigation of a non-linear model of a wind-driven ocean. J. Atm. Sci., 20, 594.

Carrier, G.F., & Robinson, A.R. 1962. On the theory of the wind-driven ocean circulation. J. Fluid Mech., 12, 49.

Charney, J. 1955. The Gulf Stream as an inertial boundary layer. Proc. Nat. Acad. Sci. Wash., 41, 731.

Fofonoff, N.P. 1954. Steady flow in a frictionless homogeneous ocean. Jour. Mar. Res., 13, 254.

Greenspan, H.P. 1962. A criterion for the existence of inertial boundary layers in oceanic circulation. Proc. Nat. Acad. Sci., 48, 2034.

Greenspan, H.P. 1965. On the general theory of contained rotating fluid motions. J. Fluid Mech., 22, 449.

Greenspan, H.P., & Howard, L.N. 1963. On a time-dependent motion of a rotating fluid. J. Fluid Mech., 17, 385.

Holland, W.R. 1966. Wind-driven circulation in an ocean with bottom topography. Doctoral dissertation, Univ. of California, San Diego.

Ilyin, A.N., & Kamenkovich, V.M. 1963. On the influence of friction on ocean curretns. Dokl. Akad. Nauk. SSSR, 150, 1274.

Moore, D.W. 1963. Rossby waves in ocean circulation. Deep-Sea Res., 10, 735.

Lilly, D.K, 1966. On the instability of Ekman boundary flow. J. Atm. Sci., 23, 481.

Morgan, G.W. 1956. On the wind-driven ocean circulation. *Tellus*, **8**, 301.

Munk, W.H. 1950. On the wind-driven ocean circulation. *J. Meteor.*, **7**, 79.

Munk, W.H., & Carrier, G.F. 1950. The wind-driven circulation in ocean basins of various shapes. *Tellus*, **2**, 158.

Pedlosky, J., & Greenspan, H.P. 1967. A simple laboratory model for the oceanic circulation. *J. Fluid Mech.*, **27**, 291.

Stommel, H. 1965. *The Gulf Stream*. Berkeley: Univ. of Calif. Press.

APPENDICES

APPENDIX A

Numerical Evaluation of Theoretical
Interior Pressure Field

The theoretical interior pressure field (17) was evaluated by the following method on the IBM 7094 digital computer at the M.I.T. Computation Center. A FORTRAN II-coded function subprogram called NYU BES61 (SDA #3177) was simplified to compute the function

$$i_m(x) = e^{-x} I_m(x) \qquad (A1)$$

for x real and positive non-zero, and m a positive integer. The computing scheme utilized a recurrence technique when $x < 10$ and the asymptotic phase amplitude method when $x \geqslant 10$, giving an average accuracy of 6 to 7 significant figures.

Substitution of this function into the interior pressure equation gave the following series to be evaluated:

$$\frac{p(r,\theta)}{a^2} = \frac{r\cos\theta}{\Gamma} - e^{-\Gamma(r\cos\theta - 1)} \left\{ \frac{i_1(\Gamma)}{\Gamma i_0(\Gamma)} i_0(\Gamma r) + \sum_{m=1}^{M} \frac{i_{m+1}(\Gamma) + i_{m-1}(\Gamma)}{\Gamma i_m(\Gamma)} i_m(\Gamma r)\cos m\theta \right\} \qquad (A2)$$

The convergence criteria used to pick the terminal value of m utilizes the monotonic decay of $i_m(x)$ as $m \to \infty$. Since the maximum number of terms in the series is needed in the western half of the circle ($x < 0$) where the exponential factor in equation A-2 becomes large, the series was summed at the westernmost point ($r = 1$, $\theta = \pi$) until the criteria

$$\left| e^{-2r} - i_0 + 2\sum_{p=1}^{m_*} (-1)^{p+1} i_p(\Gamma) \right| \leqslant \epsilon \qquad (A3)$$

based on the imposed condition that $p = 0$ on the boundary was satisfied. Since $i_m(x)$ decays monotonically with increasing m, the remaining terms are not significant if ϵ is suitably chosen. The series was then summed to $M = m_*$ on a 9 x 9 semicircular grid. If the computed values of p/a^2 on the rest of the western boundary points exceeded 10^{-3}, the series was resummed to include n_* additional terms. Table A 1 lists the values of Γ, M, m_*, n_*,

used and the maximum deviation from 0 observed on the boundary.

Γ	M_*	m_*	n_*	ϵ	maximum deviation from 0 on boundary
.2	3	3	0	10^{-6}	10^{-3}
.6	4	4	0	10^{-5}	10^{-3}
1.0	5	5	0	10^{-5}	7×10^{-4}
2.0	7	7	0	10^{-5}	7×10^{-4}
3.0	12	9	3	10^{-6}	$< 10^{-4}$
5.0	17	12	5	10^{-6}	$< 10^{-4}$

TABLE A 1.

Parameter Values and Deviation of Boundary
Values for the Numerical Evaluation of the Interior
Linear Inviscid Pressure Function(17)

APPENDIX B

Calculation of Azimuthal Velocity Profile

The azimuthal velocity profiles were obtained from flow photographs (similar to Plate 1) by the following method. A sequence of at least 8 dye pulses was photographed in each western boundary layer velocity experiment. An 8x enlargement was made of each 35mm negative by an Itek reader-printer and the copy digitized with a Wayne-George X-Y Coordinate digital converter. The copy was oriented approximately on the digitizer bed as indicated in the figure below. The electrode was stretched along a diameter of the cylinder, so the line segment P_1P_2 was used to locate the cylinder axis P_3. After measuring the coordinate values of P_1 and P_2, the tracer was advanced from P_1 along the leading edge of the two dye pulses (C_1 and C_2) measuring the y coordinate value for every $\Delta x = 0.1''$ incremental advance. The card output was checked for punching errors before processing on the IBM 360 digital computer at the M.I.T. Computation Center.
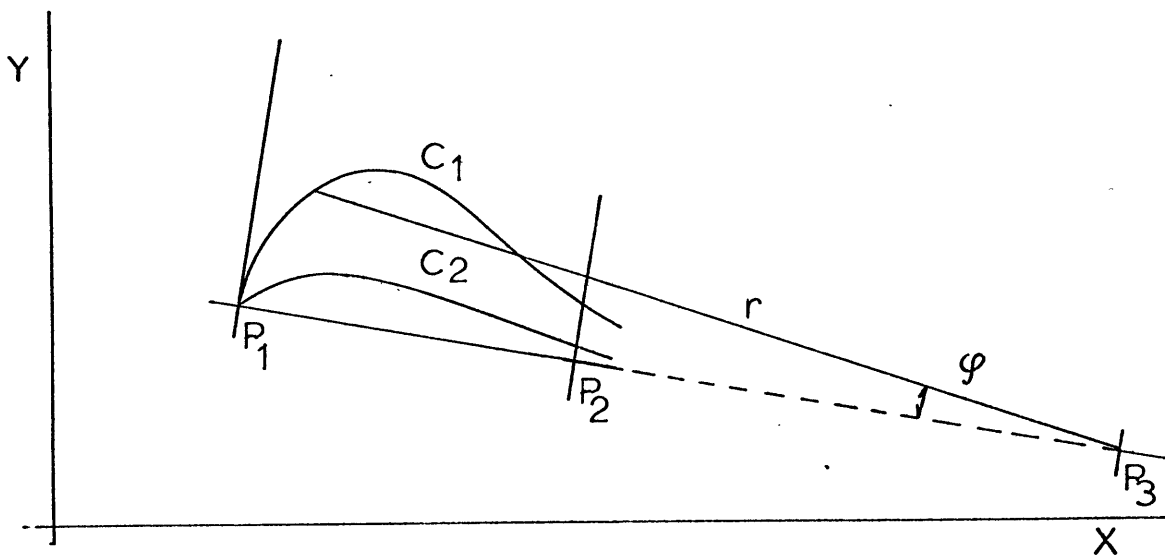
The program computed P_3 from the direction and known magnitude of $\overrightarrow{P_1P_2}$. Then the x, y coordinates of points on both curves were transformed, using algebra, into the polar coordinates Λ and $\mathcal{G}$. A linear interpolation scheme was used to determine values $\mathcal{G}_1(\Lambda)$ and $\mathcal{G}_2(\Lambda)$ for both curves at a number of radial positions. The average integrated velocity was then calculated at the radial positions $\{\Lambda_n\}$ from the equation

$$U(\Lambda_n) = \frac{(\mathcal{G}_1 - \mathcal{G}_2)}{\Delta t} \Lambda_n \qquad (B1)$$

This equation will give an unbiassed estimate of the true azimuthal velocity provided (a) the ratio of radial to tangential velocities is negligible and (b) v is constant over the small arc measured. Since $O(|u|/|v|) \sim E^{1/3}/\tan\alpha \sim .05$ and v was approximately stationary near $\theta = \pi$, (B-1) provides a good estimate of the instantaneous azimuthal velocity evaluated at the average azimuthal position. This estimate was of course more biassed where v was changing rapidly with θ. A better comparison with the observed values could be made by using the theoretical velocity field to compute the left hand side of (B-1).

APPENDIX C

Experimental Apparatus

C-1. Fluid Container

The fluid container consists of a hollow Plexiglass cylinder rebored to an inner radius of $12.700 \pm .005$ cm and capped on both ends with circular Plexiglass plates. A false top and bottom inserted inside the cylinder form the "sliced cylinder" geometry. However, to simplify the design, the usual geometry has been inverted with the top sloping and horizontal bottom plate driven relative to the rest of the basin.

Three sloping bottoms were machined from 0.92 cm thick Plexiglass plate stock using a sloping bed rotary milling table. This procedure gave the correct geometrical shape without marking either top or bottom surface. The upper surface was flat to within $\pm .003$ cm variation over its area and was left untouched to ensure maximum transparency. The sloping bottoms bolt to a stainless steel knob set in a 0-ring bearing in the top plate aligned along the cylinder's axis. This design allowed the orientation of the sloping bottom relative to the fixed cylinder and electrode grid to be changed easily. The average separation between the cylinder wall and sloping bottom is 0.025 cm, approximately 45% of the Ekman layer thickness $LE^{1/2}$.

C-2. Disk and Drive.

The driving top is a 0.61 cm thick glass plate ground to a radius of 12.675 .cm. The plate is optically flat and its surfaces parallel. The average wall clearance is again 0.025 cm. Originally a stock unground Plexiglass plate was used but its small 0.025 cm surface variations were found to cause a noticeable flow disturbance.

Three miniature stainless steel ball bearings support the glass disk and thus determine its plane of rotation. The height of each bearing was adjusted to set the plane perpendicular to the table rotation axis.

A three legged stainless steel yoke is mounted approximately

on center on the lower surface of the glass disk. The disk is driven via a simple universal joint, consisting of a slotted receptacle in the yoke and a pinned shaft. This keeps the disk's plane of rotation constant despite small shaft misalignment and runout. An oilite bronze bearing with rubber water seal mounted on center in the cylinder's bottom plate centers and supports the vertical stainless steel shaft. It is turned on by a 150 oz.-in. Hurst synchronous motor through a precision P.I.C. component worm and spur gear train mounted on the turntable. Electrical power is supplied through an impedence match by an audio oscillator and amplifier system (hp 200 CD oscillator, Dynaco Mark IV amplifier). The relative angular velocity of the glass disk could be varied by a change in either the gear reduction ratio or the oscillator frequency. The overall drive train was designed to mimimize backlash and the disk's rotational stability over 1 period is estimated at $\frac{\delta \epsilon \Omega}{\epsilon \Omega} \leqslant 2 \times 10^{-5}$.

C-3. Turntable and Drive

The fluid container is mounted on three supporting blocks above the turntable surface, allowing the cylinder axis and table rotation axis to be aligned to within ±.005 cm in the radial direction and within ±40 seconds of arc in the vertical direction.

The turntable itself consisted of a 30" diameter steel disk mounted on a 5" outside diameter hollow steel shaft. Its principal momentum of inertia is 37×10^2 slug inch^2. The bearing system utilizes an angular thrust bearing to support the table weight and a lighter radial bearing mounted about 12 inches below the other to center the table. The bearing seats bolt to a massive turntable base which rests on combination wood-foam rubber damping pads on the laboratory floor.

The turntable is driven by a ¼ hp Louis Allis synchronous 3-phase motor through a Graham variable speed transmission and direct drive coupling. The vertical output shaft from the transmission turns the lower of two universal joints mounted back to back on a splined shaft, the upper universal attaching to the turntable shaft. This design allows an angular distortion-free rotation of transmission and table while isolating the table from motor and transmission noise.

The Graham unit (model N29W25) was factor fitted with matched

parts to improve its rotational stability. Its rated peak to peak variability is $\frac{\delta\Omega}{\Omega} \leq 2 \times 10^{-4}$. The table's angular velocity is determined by measuring an individual rotation period with an electronic timer. A small collinated d.c. light source mounted on the table triggers a light-activated silicon-controlled rectifier in a variable pulse width "single shot" delay circuit, sending a large amplitude square wave pulse to a Beckman timer, model 5230. At the light level used, the circuit turn-on time is ~ 10 μsec which ensures an overall measurement accuracy of $\frac{\epsilon_T}{T} \leq 1 \times 10^{-5}$. The measured turntable stability is $\frac{\sigma_T}{T} \leq 2 \times 10^{-4}$. Additional information on the turntable design and construction is contained in a laboratory report (Beardsley, 1967).

C-4. Support Equipment

Flow observations were obtained using sequence or lapsed time photography. A 22 watt flourescent circle lamp with parabolic reflector is mounted on the turntable beneath the fluid container to provide back lighting. The camera, a Nikon 35mm with f/1.9 lens and motorized back, is attached to a rectangular frame built with channel pipe around the fluid container and bolted to the table. A battery power pack drives the camera mechanism through a set of microswitches activated by a Cramer timer (model 540). The fractional variability of the switching pulses is $\sim 1 \times 10^{-3}$. Both battery pack and timer are mounted on the table.

The fluid temperature is measured with a copper-constantin thermocouple attached to the side wall in the fluid container. The reference junction and icebath are also mounted on the table to reduce stray emf pick-up across the copper slip rings. These have also been electrically and thermally shielded. The accuracies of the temperature and viscousity measurements are $\pm .02^{\circ}$ C (~ 1 μV) and ± 0.006 centistokes respectively. A schematic of the support equipment is shown in Fig. C 1.

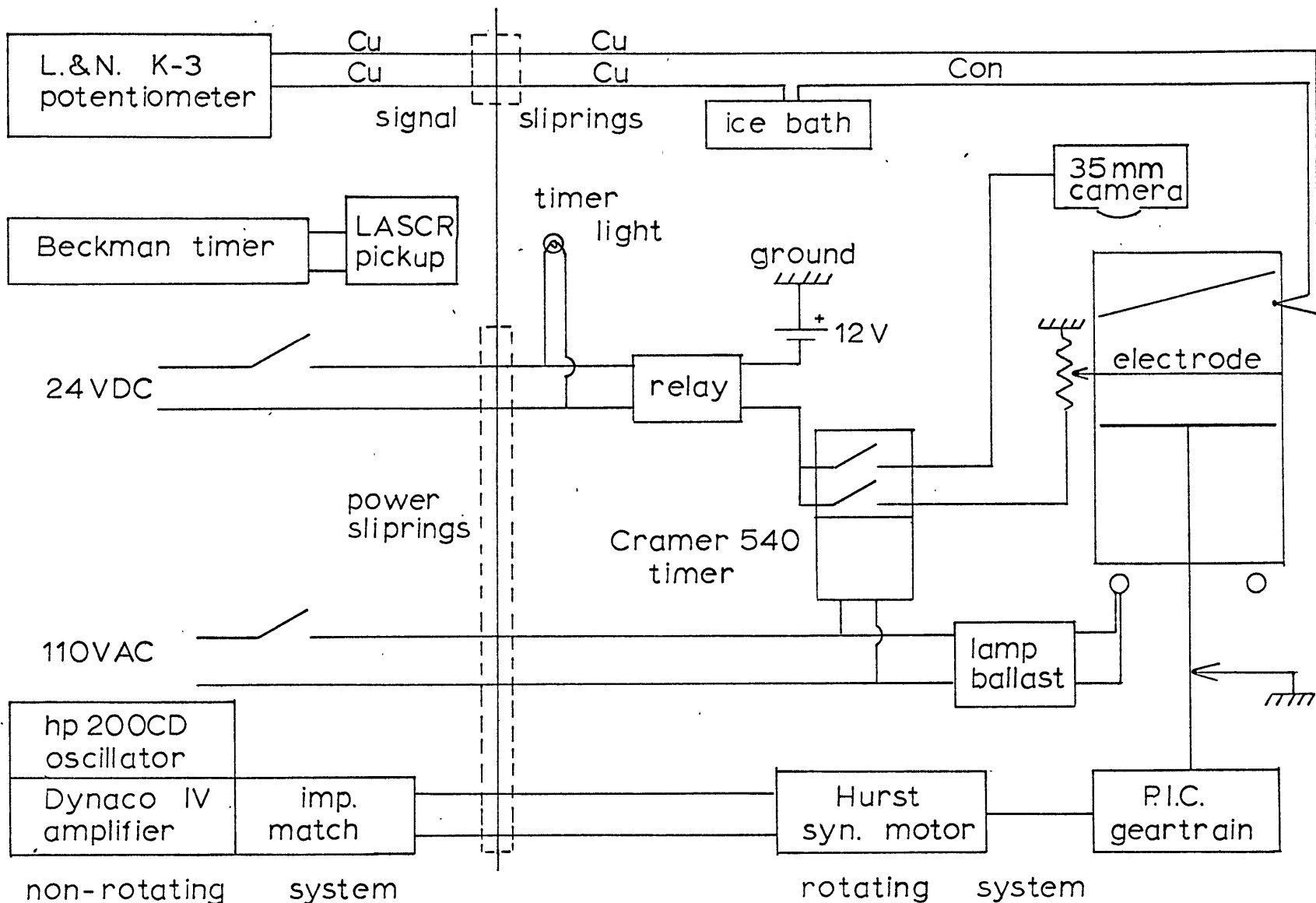FIGURE C 1.   Schematic of support equipment

APPENDIX D

Tabulation of Results for the Stability Study

Run #	E	Re	ϵ	$\tan\alpha$	State	T
7-2	2.110	80.28	-.0650	.178±.003	US	25.6±3.2
7-3	2.105	93.82	-.0759	.178±.003	US	25.6±3.2
8-1	2.100	53.64	-.0433	.178±.003	S	
8-2	2.097	64.41	-.0520	.178±.003	S	
9-1	2.092	75.23	-.0607	.178±.003	S	
9-2	2.087	86.09	-.0694	.178±.003	US	22.8±1.1
10-1	2.085	43.07	-.0347	.178±.003	S	
10-2	2.080	29.81	-.0240	.178±.003	S	
11-1	2.083	74.47	-.0599	.178±.003	S	
11-2	2.080	86.93	-.0699	.178±.003	US	23.4±1.3
12-1	2.076	74.60	-.0599	.178±.003	S	
12-2	2.072	87.02	-.0699	.178±.003	US	22.4±0.7
19-1	1.956	79.90	-.0623	.178±.003	US	24.5±1.4
19-2	1.956	80.57	-.0628	.178±.003	US	25.2±1.6
22-2	1.949	73.78	-.0574	.178±.003	S	
26-1	2.048	78.73	-.0628	.178±.003	US	24.5±0.7
26-2	2.045	80.15	-.0639	.178±.003	US	25.2±1.1
27-1	2.087	75.33	-.0607	.178±.003	S	
27-2	2.085	76.59	-.0617	.178±.003	S	
29-2	2.063	79.83	-.0639	.178±.003	US	26.0±0.7
30-1	6.220	114.07	-.1586	.178±.003	US	12.2±1.6
31-2	6.188	91.60	-.1271	.178±.003	S	
31'-1	6.167	110.68	-.1533	.178±.003	US	12.2±1.6
33-2	6.082	102.17	-.1405	.178±.003	S	
33'-1	6.135	110.55	-.1527	.178±.003	US	
35-2	6.104	105.58	-.1454	.178±.003	S	
36-1	6.099	107.74	-.1484	.178±.003	US	12.2±1.6
36'-2	6.214	108.60	-.1510	.178±.003	US	12.2±2.6
37-1	6.189	107.68	-.1494	.178±.003	US	12.9±2.6
38-1	3.777	84.99	-.0924	.178±.003	S	
38-2	3.772	87.84	-.0954	.178±.003	S	
39-1	3.767	89.35	-.0970	.178±.003	S	

Run #	E	Re	ϵ	tan α	State	T
39-2	3.717	89.64	-.0967	.178±.003	S	
40-1	3.704	94.38	-.1016	.178±.003	US	16.2±2.0
40-2	3.694	98.25	-.1056	.178±.003	US	16.2±1.0
41-1	3.696	97.19	-.1045	.178±.003	US	16.2±0.7
41-2	3.695	97.89	-.1053	.178±.003	US	16.2±0.5
42-1	3.870	92.16	-.1014	.178±.003	US	16.2±2.0
42-2	3.868	94.16	-.1036	.178±.003	US	16.2±2.0
42-3	3.865	96.12	-.1057	.178±.003	US	
43-1	1.275	63.10	-.0399	.178±.003	S	
43-2	1.274	64.07	-.0405	.178±.003	S	
44-1	1.282	73.28	-.0464	.178±.003	US	28.2±1.0
44-2	1.281	68.80	-.0436	.178±.003	S	
45-1	1.256	76.23	-.0478	.178±.003	US	28.2±1.0
45-2	1.256	74.85	-.0469	.178±.003	US	28.2±1.0
46-1	1.255	74.03	-.0464	.178±.003	US	30.2±1.0
46-2	1.259	72.93	-.0457	.178±.003	US	30.5±0.8
47-1	1.253	72 00	-.0451	.178±.003	S	
47-2	1.252	71.00	-.0449	.178±.003	S	
48-1	2.127	79.50	-.0527	.144±.003	S	
48-2	2.129	87.51	-.0580	.144±.003	S	
49-1	2.160	105.12	-.0702	.144±.003	US	23.1±0.9
49-2	2.160	100.47	-.0671	.144±.003	US	24.5±0.9
50-1	2.150	103.08	-.0687	.144±.003	US	23.8±1.2
50-2	2.149	97.52	-.0650	.144±.003	S	
51-1	2.131	98.52	-.0654	.144±.003	S	
51-2	2.129	99.56	-.0660	.144±.003	S	
52-1	2.118	134.28	-.0686	.111±.003	US	21.6±0.9
52-2	2.124	126.64	-.0648	.111±.003	S	
53-1	2.134	131·73	-.0675	.111±.003	US	23.8±1.2
53-2	2.133	130.27	-.0667	.111±.003	S	
54-1	2.147	121 54	-.0625	.111±.003	S	
54-2	2.148	133.92	-.0689	.111±.003	US	22.5±1.5

APPENDIX E

Derivation of an Equivalent Two-Dimensional Problem for the Sliced-Cylinder Geometry

We may easily derive an approximate two-dimensional vorticity equation for the sliced cylinder model on the assumptions that (a) the horizontal flow is independent of z in the interior and western boundary layer and (b) the vertical Ekman layer flux on both top and bottom disks is correctly given by the compatibility condition (3). The momentum and continuity equations, scaled in the usual manner,

$$\vec{u} = \frac{\vec{u}^*}{\epsilon \Omega L} \qquad h = \frac{h^*}{L} \qquad p = \frac{p^*}{\rho \epsilon (\Omega L)^2} \qquad \frac{\partial}{\partial t} = \frac{1}{\Omega} \frac{\partial}{\partial t^*}$$

simplify to

$$u_t + \epsilon \{ u u_x + v u_y \} - 2v = -p_x + E \Delta u$$

$$v_t + \epsilon \{ u v_x + v v_y \} + 2u = -p_y + E \Delta v$$

$$u_x + v_y + w_z = 0$$

The curl of the momentum components yields the vorticity equation

$$S_t + \epsilon \{ u S_x + v S_y \} + (2 + \epsilon S)(u_x + v_y) = E \Delta S$$

where $S = v_x - u_y$

By our assumptions, the integrated horizontal divergence is

$$\int_{\tan \alpha y}^{1} (u_x + v_y) \, dz = (u_x + v_y) h = w (\tan \alpha y) - w(1)$$

Since $h = 1 - \tan \alpha y$ and

$$\omega(\tan\alpha y) = \tan\alpha \, v + \frac{E^{1/2} \varsigma}{2} + O(E^{1/2}\tan\alpha)$$

$$\omega(1) = E^{1/2} - \frac{E^{1/2}\varsigma}{2}$$

the local horizontal divergence is

$$(u_x + v_y) \simeq \frac{1}{h}\left\{\tan\alpha \, v + E^{1/2}\varsigma - E^{1/2}\right\}$$

The vertical vorticity balance is then

$$\varsigma_t + \epsilon\left(u\varsigma_x + v\varsigma_y\right) + \left(\frac{2+\epsilon\varsigma}{h}\right)\left(\tan\alpha v + E^{1/2}\varsigma - E^{1/2}\right) = E\Delta\varsigma \quad (E\text{-}1)$$

Introduction of a vertically integrated vorticity function $\bar{\varsigma}$

$$\bar{\varsigma} = \int_{\tan\alpha y}^{1} \varsigma \, dz = \varsigma(1 + \tan\alpha y)$$

and some computation further simplifies (E-1) to

$$\overbrace{\bar{\varsigma}_t + \epsilon\left(u\bar{\varsigma}_x + v\bar{\varsigma}_y\right)}^{a} + \overbrace{\frac{2\tan\alpha \, v\bar{\varsigma}}{h}}^{b} + \overset{c}{2(\tan\alpha v} + \overset{d}{\frac{E^{1/2}\bar{\varsigma}}{h})} = \overset{e}{(2} + \overset{f}{\frac{\epsilon\bar{\varsigma}}{h})E^{1/2}}$$

$$+ E\left(\overset{g}{\Delta\bar{\varsigma}} + \overset{h}{2\tan\alpha\bar{\varsigma}_y} + \overset{i}{2\tan^2\alpha\frac{\bar{\varsigma}}{h}}\right) \quad (E\text{-}2)$$

The secondary vertical circulation driven by the upper Ekman
layer (term e in E-2) is the vorticity source and as the only
forcing term in (E-2) corresponds to the "surface stress" or
"equivalent body force" used in the theoretical wind-driven
ocean circulation model studies. The interior balance $c = e$
determines the velocity and vorticity scales

$$V_s = \frac{E^{1/2}}{\tan\alpha}$$

$$(u,v) = \frac{E^{1/2}}{\tan\alpha}(u', v') \quad (E\text{-}3)$$

$$\bar{\varsigma} = E^{1/2}\varsigma' \quad (E\text{-}4)$$

so that u', v', and ς' are $O(1)$ dimensionalless fields in the
interior region. Substitution of (E-3) and (E-4) into the

vorticity equation (E-2) and ignoring the smaller terms (b, d, f, h, and i) finally yield an approximate scaled vorticity equation

$$\varsigma_t' + \frac{\epsilon E^{\frac{1}{2}}}{\tan\alpha}\left\{u'\varsigma_x' + v'\varsigma_y'\right\} + 2v' = 2 + E\Delta\varsigma'$$

This may be compared directly to the scaled vorticity equation (2.3) used by Bryan (1963)

$$\frac{\partial}{\partial T}\nabla^2\psi + \epsilon\left[\frac{\partial}{\partial y}\left(\frac{\partial\psi}{\partial x}\nabla^2\psi\right) - \frac{\partial}{\partial x}\left(\frac{\partial\psi}{\partial y}\nabla^2\psi\right)\right] + \psi_x = -\sin\frac{\pi y'}{2} + \frac{\epsilon}{Re}\nabla^4\psi$$

which was scaled according to the relations

$$(x', y') = L(x, y) \qquad t = \frac{T}{\beta L}$$

$$\psi' = \rho h L V_s \psi$$

$$V_s = \frac{\tau_0\pi}{2\beta L\rho h}$$

The equivalent Rossby and Ekman numbers for Bryan's results are then determined from the relations

$$\frac{\epsilon_{sc} E_{sc}^{\frac{1}{2}}}{\tan\alpha} = \epsilon_{\beta\text{-plane}}$$

$$E_{sc} = \epsilon_{\beta\text{-plane}}/Re_{\beta\text{-plane}}$$

where $Re_{\beta\text{-plane}}$ corresponds to the interior Reynolds number $\epsilon_{sc}/\tan\alpha\, E^{\frac{1}{2}}$. The equivalent parameter values used in Bryan's study are tabulated below.

β- plane Study			Sliced Cylinder Parameters	
	Re	Flow State	E	Re
3.2×10^{-4}	100	unstable	3.2×10^{-6}	10
3.2×10^{-4}	60	stable	5.43×10^{-6}	60
1.28×10^{-3}	60	stable	2.14×10^{-5}	60
1.28×10^{-3}	40	stable	3.20×10^{-5}	40
1.28×10^{-3}	20	stable	6.40×10^{-5}	20
1.28×10^{-3}	5	stable	2.56×10^{-4}	5

Biographical Note

The author was born in Jacksonville, Florida, on January 28, 1942. He attended public high school in Washington, D.C., and entered M.I.T. as a freshman in September, 1960. He graduated from M.I.T. in June, 1964, with a B.S. in physics, the title of his undergraduate thesis being "The Diffusion of Radon in Surface Soil".

The author entered the geology and geophysics department at M.I.T. as a graduate student in September, 1964. He was the recipient of the N.S.F. Cooperative Fellowship and later the Hertz Hellowship. He spent the summer of 1966 at the Woods Hole Oceanographic Institute as a participant in its Geophysical Fluid Dynamics seminar.

The author is presently a member of Sigma Xi and the American Geophysical Union.